

Density-Functional Theory Investigation of the Geometric, Energetic, and Optical Properties of the Cobalt(II)tris(2,2'-bipyridine) Complex in the High-Spin and the Jahn–Teller Active Low-Spin States

Alfredo Vargas,[†] Mohamed Zerara,[†] Elmars Krausz,[‡] Andreas Hauser,^{†,*} and Latévi Max Lawson Daku^{†,*}

Département de Chimie Physique, Université de Genève, 30 quai Ernest-Ansermet, CH-1211 Genève 4, Switzerland, and Research School of Chemistry, Australian National University, Building 31 Science Road, Canberra ACT 0200, Australia

Received April 13, 2006

Abstract: State-of-the-art generalized gradient approximation (GGA) (PBE, OPBE, RPBE, OLYP, and HCTH), meta-GGA (VSXC and TPSS), and hybrid (B3LYP, B3LYP*, O3LYP, and PBE0) functionals are compared for the determination of the structure and the energetics of the D_3 $[\text{Co}(\text{bpy})_3]^{2+}$ complex in the $^4\text{A}_2$ and ^4E trigonal components of the high-spin $^4\text{T}_{1g}(\text{t}_{2g}^5 \text{e}_g^2)$ state and in the low-spin ^2E state of octahedral $^2\text{E}_g(\text{t}_{2g}^6 \text{e}_g^1)$ parentage. Their comparison extends also to the investigation of the Jahn–Teller instability of the ^2E state through the characterization of the extrema of C_2 symmetry of this spin state's potential energy surface. The results obtained for $[\text{Co}(\text{bpy})_3]^{2+}$ in either spin manifold are very consistent among the functionals used and are in good agreement with available experimental data. The functionals, however, perform very differently with respect to the spin-state energetics because the calculated values of the high-spin/low-spin energy difference $\Delta E_{\text{HL}}^{\text{el}}$ vary between -3212 and 3919 cm^{-1} . Semilocal functionals tend to give too large $\Delta E_{\text{HL}}^{\text{el}}$ values and thus fail to correctly predict the high-spin state as the ground state of the isolated complex, while hybrid functionals tend to overestimate the stability of the high-spin state with respect to the low-spin state. Reliable results are, however, obtained with the OLYP, HCTH, B3LYP*, and O3LYP functionals which perform best for the description of the isolated complex. The optical properties of $[\text{Co}(\text{bpy})_3]^{2+}$ in the two spin states are also analyzed on the basis of electronic excitation calculations performed within time-dependent density functional response theory. The calculated absorption and circular dichroism spectra agree well with experimental results.

1. Introduction

The electronic ground state of octahedral d^7 complexes is either the high-spin (HS) $^4\text{T}_{1g}(\text{t}_{2g}^5 \text{e}_g^2)$ state or the low-spin (LS) $^2\text{E}_g(\text{t}_{2g}^6 \text{e}_g^1)$ state depending on the strength of the ligand field. The d^7 $[\text{Co}(\text{bpy})_3]^{2+}$ ($\text{bpy} = 2,2'$ -bipyridine) complex

is an intermediate-field complex with normally a HS ground state and a low-lying excited LS state. However, when $[\text{Co}(\text{bpy})_3]^{2+}$ is incorporated into zeolite-Y supercages^{1–3} or into the cavities of three-dimensional oxalate networks,^{4,5} the LS state becomes the ground state and the complex exhibits spin crossover. The X-ray structures of the complex in the HS and LS states⁴ show a large difference of the metal–ligand bond length, $\Delta r_{\text{HL}} = r_{\text{HS}} - r_{\text{LS}}$, of as much as $\sim 0.1 \text{ \AA}$, which is due to the fact that the change of spin state involves an electron transfer between the metallic nonbond-

* Corresponding author e-mail: max.lawson@unige.ch (L.M.L.D.), andreas.hauser@unige.ch (A.H.).

[†] Université de Genève.

[‡] Australian National University.

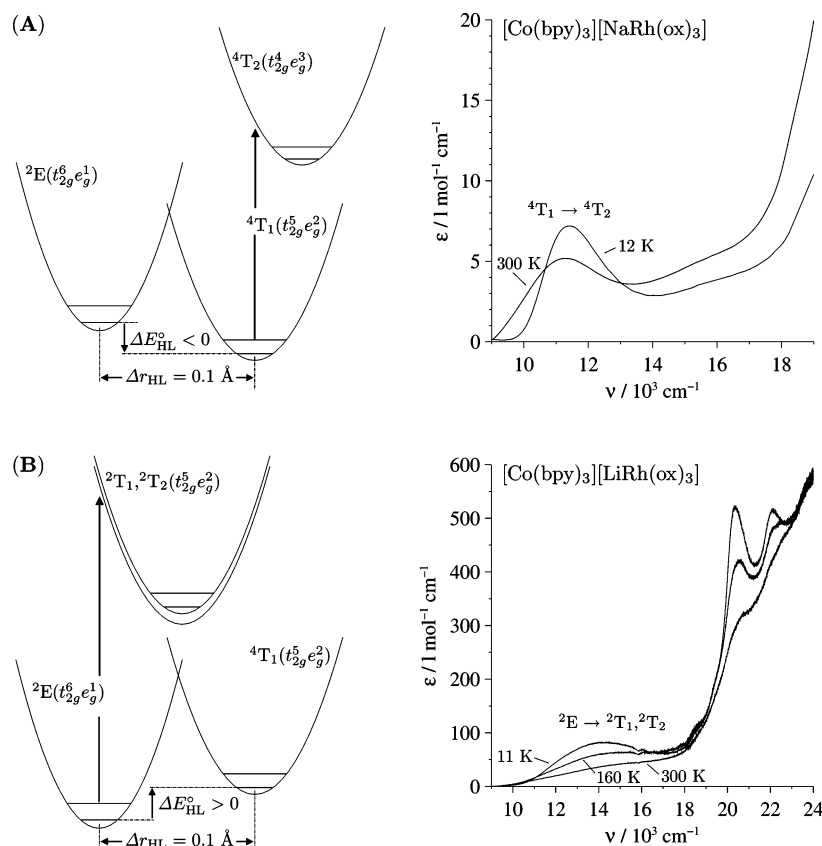


Figure 1. (A) Configurational coordinate diagram for the HS [Co(bpy)₃]²⁺ complex along the Co–N totally symmetric normal mode and temperature-dependent single-crystal absorption spectra of the HS compound [Co(bpy)₃][NaRh(ox)₃]. (B) Configurational coordinate diagram for the LS [Co(bpy)₃]²⁺ complex and temperature-dependent single-crystal absorption spectra of the spin-crossover compound [Co(bpy)₃][LiRh(ox)₃].

ing t_{2g} and antibonding e_g orbitals. The change of spin states is therefore accompanied by a variation of the molecular volume, $\Delta V_{\text{HL}} = V_{\text{HS}} - V_{\text{LS}}$, estimated to $\sim 17 \text{ \AA}^3$.⁵ The molecular volume of the complex being larger in the HS state than in the LS state, the observed inversion of the energetic order of the two spin states can be rationalized in terms of an internal or chemical pressure exerted by the confining environment of the hosts on the [Co(bpy)₃]²⁺ guest which destabilizes the HS state with respect to the LS state.^{4,5} Figure 1 helps illustrate this phenomenon: in [Co(bpy)₃][NaRh(ox)₃] (Figure 1A), the complex has a classic HS electronic ground state, as shown in the configurational diagram along the Co–N distance coordinate. The zero-point energy E_{LS}° of the LS state is only slightly higher than the zero-point energy E_{HS}° of the HS state ($\Delta E_{\text{HL}}^{\circ} = E_{\text{HS}}^{\circ} - E_{\text{LS}}^{\circ} < 0$). The population of the HS state being favored by the entropy, this state remains the only populated state at all temperatures, in accordance with the temperature-dependent single-crystal absorption spectra which are typical for the HS species. On passing to [Co(bpy)₃][LiRh(ox)₃] (Figure 1B), the size of the cavity occupied by [Co(bpy)₃]²⁺ is reduced because of the substitution of the Na⁺ by the smaller Li⁺ cations on the oxalate backbone. The resulting increase in the chemical pressure exerted onto the complex destabilizes the HS state with respect to the LS state sufficiently for [Co(bpy)₃]²⁺ to become a spin-crossover complex ($\Delta E_{\text{HL}}^{\circ} > 0$). The low-temperature (12 K) absorption spectrum is typical for the LS species; the spectra recorded at

higher temperatures allow one to follow the entropy-driven thermal transition to the HS state.

Although the concept of chemical pressure provides insight into the manner in which the electronic properties of transition-metal complexes can be tuned by the guest–host interactions,⁶ it does not provide a detailed picture of the involved interactions. The use of quantum chemical methods should help improve our understanding of such guest–host interactions. However, prior to the investigation of these interactions for [Co(bpy)₃]²⁺ incorporated in the cavities of zeolite Y or oxalate networks, the ability of such methods to provide an accurate description of the isolated complex has to be examined.

For the present study of [Co(bpy)₃]²⁺, methods based on density functional theory (DFT) only were considered, because the large number of atoms in the complex precludes the use of computationally demanding high-level ab initio methods. The calculations were performed within the Kohn–Sham (KS) formulation of spin-density functional theory,^{7–12} wherein the ground-state energy E_0 of an N -electron system in an external local potential $v(\mathbf{r})$ is expressed as a functional of the spin-up $\rho_{\uparrow}(\mathbf{r})$ and spin-down $\rho_{\downarrow}(\mathbf{r})$ densities as in eq 1. $\rho(\mathbf{r}) = \rho_{\uparrow}(\mathbf{r}) + \rho_{\downarrow}(\mathbf{r})$ is the charge density; $T_s[\rho_{\uparrow}, \rho_{\downarrow}]$ is the

$$E_0[\rho_{\uparrow}, \rho_{\downarrow}] = T_s[\rho_{\uparrow}, \rho_{\downarrow}] + \frac{1}{2} \int d\mathbf{r} d\mathbf{r}' \frac{\rho(\mathbf{r}) \rho(\mathbf{r}')}{|\mathbf{r} - \mathbf{r}'|} + \int d\mathbf{r} \rho(\mathbf{r}) v(\mathbf{r}) + E_{\text{xc}}[\rho_{\uparrow}, \rho_{\downarrow}] \quad (1)$$

kinetic energy of the KS noninteracting N -electron system with the same spin densities as those of the interacting system and is given by eqs 2 and 3

$$T_s[\rho_\uparrow, \rho_\downarrow] = \int d\mathbf{r} [\tau_\uparrow(\mathbf{r}) + \tau_\downarrow(\mathbf{r})] \quad (2)$$

$$\tau_\sigma(\mathbf{r}) = \frac{1}{2} \sum_i f_{i\sigma} |\nabla \psi_{i\sigma}(\mathbf{r})|^2 \quad (3)$$

with $\sigma = \uparrow, \downarrow$, $f_{i\sigma}$ and $\psi_{i\sigma}(\mathbf{r})$ are the occupation number and the spin orbital of the i th σ -type single-particle level of the KS noninteracting system.

The exchange-correlation (XC) energy, $E_{xc}[\rho_\uparrow, \rho_\downarrow]$, is the sum of the exchange and the correlation energy, $E_x[\rho_\uparrow, \rho_\downarrow]$ and $E_c[\rho_\uparrow, \rho_\downarrow]$, respectively, for which approximate functionals are devised, requiring that either the largest number of the mathematical properties of the exact exchange and correlation functionals or, at least, a few conditions known to be limiting for the evaluation of selected properties are satisfied. The approximate XC functionals of widespread use either belong to the family of local and semilocal approximations or are hybrid functionals. Local and semilocal functionals admit the general form given in eq 4.

$$E_{xc}[\rho_\uparrow, \rho_\downarrow] = \int d\mathbf{r} \rho(\mathbf{r}) \epsilon_{xc}(\rho_\uparrow(\mathbf{r}), \rho_\downarrow(\mathbf{r}), \nabla \rho_\uparrow(\mathbf{r}), \nabla \rho_\downarrow(\mathbf{r}), \nabla^2 \rho_\uparrow(\mathbf{r}), \nabla^2 \rho_\downarrow(\mathbf{r}), \tau_\uparrow(\mathbf{r}), \tau_\downarrow(\mathbf{r})) \quad (4)$$

ϵ_{xc} is the XC energy *per* particle. In the early local density approximation (LDA),^{8,13–16} it only depends on the spin densities. Despite being valid only for slowly varying densities, the LDA performs reasonably well for the description of atomic and molecular systems, but the accuracy of energy parameters is not always sufficient.

Semilocal approximations improve on the LDA by including corrections which reflect the strongly inhomogeneous densities of real systems. Thus, within the generalized gradient approximation (GGA), ϵ_{xc} depends on the spin densities but also on their gradients $\nabla \rho_\sigma(\mathbf{r})$. The GGA outperforms the LDA,^{17–20} and this nowadays more than compensates for the increase in the computation time tied to the evaluation of the gradients. The meta-generalized gradient approximation (meta-GGA) goes beyond the GGA in that ϵ_{xc} becomes also a function of the second derivatives of the spin densities $\nabla^2 \rho_\sigma(\mathbf{r})$ or the kinetic energy densities $\tau_\sigma(\mathbf{r})$, or of both. Although the evaluation of the semilocal variables incurs a further increase in the computational time as compared to the GGA, their inclusion allows the enrichment, in a straightforward manner, of the built-in physics of the approximate functionals (see refs 21–24). Hybrid functionals^{25,26} are characterized by the fact that they include a contribution of the exact-exchange or Hartree–Fock (HF) exchange energy $E_x^{\text{HF}}[\rho_\uparrow, \rho_\downarrow]$ given by eq 5.

$$E_x^{\text{HF}}[\rho_\uparrow, \rho_\downarrow] = -\frac{1}{2} \sum_{\sigma=\uparrow, \downarrow} \int d\mathbf{r} d\mathbf{r}' \frac{|\sum_{i\sigma} f_{i\sigma} \psi_{i\sigma}(\mathbf{r}) \psi_{i\sigma}^*(\mathbf{r}')|^2}{|\mathbf{r} - \mathbf{r}'|} \quad (5)$$

The evaluation of $E_x^{\text{HF}}[\rho_\uparrow, \rho_\downarrow]$ and the presence of the nonlocal exchange operator in the KS equations put the compu-

tational demand of the hybrid methods on the same level as that for the HF method. Note that the correct contribution of exact exchange in the hybrids is the subject of ongoing studies.^{27–29} The commonly admitted value is around 25% as in the B3LYP^{26,30} and PBE0 (also known as PBE1PBE)^{27,29,31,32} functionals. Dropping the explicit reference to the spin densities in the expression of the functionals, the B3LYP hybrid is given by eq 6

$$E_{xc}^{\text{B3LYP}} = (1 - a_0)E_x^{\text{LDA}} + a_0E_x^{\text{HF}} + a_x\Delta E_x^{\text{B}} + (1 - a_c)E_c^{\text{VWN}} + a_cE_c^{\text{LYP}} \quad (6)$$

E_c^{VWN} is the Vosko–Wilk–Nusair¹⁴ parametrization of the random phase approximation correlation energy; ΔE_x^{B} stands for Becke's 1988 gradient corrections to the LDA exchange energy,²⁰ and E_c^{LYP} is the Lee–Yang–Parr (LYP) correlation GGA.³³ The coefficients were determined by fitting to a data set of atomization energies (a_0, a_x, a_c) = (0.20, 0.72, 0.81).²⁶ The PBE0 hybrid is parameter-free and is given by eq 7

$$E_{xc}^{\text{PBE0}} = E_{xc}^{\text{PBE}} + a_0(E_x^{\text{HF}} - E_x^{\text{PBE}}) \quad (7)$$

with $a_0 = 1/4$; PBE refers to the recent XC GGA of Perdew et al.^{34,35} Although semilocal and hybrid functionals are routinely used in DFT applications, the quality that can be achieved for the description of a given property is not guaranteed to be as satisfactory as one may expect nor to increase with the degree of refinement of the functionals used.

We aim to achieve an accurate description of the structure and the energetics of $[\text{Co}(\text{bpy})_3]^{2+}$ in the LS and the HS states. In that respect, most post-LDA functionals give a very satisfactory description of the geometry of transition-metal complexes. However, they fail to reliably predict the electronic energy difference between states of different spin multiplicities, as shown in recent DFT studies performed on d^6 iron(II) complexes in the quintet HS and the singlet LS states.^{36–43} The LDA strongly overestimates the electronic HS–LS energy difference given by eq 8

$$\Delta E_{\text{HL}}^{\text{el}} = E_{\text{HS}}^{\text{el}} - E_{\text{LS}}^{\text{el}} \quad (8)$$

The situation improves with the GGA functionals, which, however, still tend to overestimate $\Delta E_{\text{HL}}^{\text{el}}$. In contrast, hybrid functionals tend to underestimate the HS–LS energy difference. The difficulties met by the approximate functionals for the evaluation of $\Delta E_{\text{HL}}^{\text{el}}$ are due to the fact that they do not properly account for the variation of exchange when the spin polarization and the metal–ligand bond length significantly vary, as is the case upon the LS \leftrightarrow HS conversion in octahedral d^4 to d^7 transition-metal complexes. Promisingly, recent functionals were reported to give satisfactory results for iron(II) complexes.^{37–43} These are the revised PBE (RPBE) XC GGA functional of Hammer et al.,⁴⁴ the OLYP functional which combines the OPTX GGA exchange of Handy and Cohen⁴⁵ with the LYP GGA correlation, and the B3LYP* reparametrized hybrid of Reiher and co-workers,^{37,38} which differs from the B3LYP by the fact that the amount of exact exchange is reduced to 15% to

allow a better description of the spin-state energetics in transition-metal complexes. Note that the study of the dependence of the calculated HS–LS energy difference in the $[\text{Fe}(\text{bpy})_3]^{2+}$ complex on the exact-exchange contribution a_0 in the PBE0 and B3LYP hybrids (eqs 6 and 7) supports the idea that this contribution should effectively be reduced to some 10%.⁴²

The fact that with regard to energy calculations the situation is very delicate requires a careful assessment of the performance of the different XC functionals for correctly predicting the HS state as the ground state of the isolated $[\text{Co}(\text{bpy})_3]^{2+}$ complex. Thus, in addition to the above-mentioned PBE, RPBE, OLYP, PBE0, B3LYP, and B3LYP* functionals, we have characterized $[\text{Co}(\text{bpy})_3]^{2+}$ in the HS and LS states, using the OPBE GGA made of the OPTX exchange and the PBE correlation functional, the HCTH (also known as HCTH/407) GGA;⁴⁶ the O3LYP hybrid, similar in form to the B3LYP, but with ΔE_x^B replaced by the OPTX gradient correction to the LDA exchange ΔE_x^{OPTX} and with reoptimized parameter values;⁴⁷ and also the VSXC⁴⁸ and TPSS²³ meta-GGAs.

The photophysical properties of $[\text{Co}(\text{bpy})_3]^{2+}$ provide clear-cut evidence for its spin state, as shown by the absorption spectra in Figure 1. The low-energy absorption bands present in the spectra of the complex in either spin state could be assigned to d–d transitions on the basis of ligand field theory (LFT).^{3,4} The higher energy bands observed for the complex in the LS state were likewise attributed to d–d transitions,³ but this assignment was later questioned.⁴ To assign these electronic transitions, we performed electronic excitation calculations within linear response theory in time-dependent density functional theory (TDDFT).^{49–52}

Our paper is organized as follows. Section 2 gives the technical details. In section 3, we present the results obtained for the geometry and the energetics of the complex in the two spin states. This includes the results obtained for the analysis of the trigonal splitting in the HS state and of the Jahn–Teller (JT) instability in the LS state. In section 4, we present the results obtained for the optical and chiroptical properties of the complex.

2. Computational and Experimental Details

The Amsterdam Density Functional (ADF)^{53,54} program package was used to perform calculations with the PBE, OPBE, RPBE, and OLYP GGAs. Calculations with the B3LYP, B3LYP*, O3LYP, and PBE0 hybrids and with the VSXC and TPSS meta-GGAs were carried out with the Gaussian program package.⁵⁵ The two packages use different types of basis sets, namely, Slater-type orbital (STO) basis sets for ADF and Gaussian-type orbital (GTO) basis sets for Gaussian. Therefore, to be able to compare the results obtained with the two package, we used for all atoms the STO TZP basis set from the ADF basis set database and the GTO TZVP basis set,⁵⁶ respectively, which both are large basis sets of valence triple- ζ polarized quality and which were shown to perform similarly for the description of $[\text{Fe}(\text{bpy})_3]^{2+}$ in the LS and HS states.⁴² To assert the similar performance of the TZP and TZVP basis sets, to which we

will refer as the \mathcal{S} and the \mathcal{G} basis sets, respectively, the Gaussian package was also used to perform calculations with the PBE GGA. Fractional occupation numbers were used in the ADF calculations but are not allowed in the present implementation of Gaussian (except as an intermediate step in the self-consistent field convergence strategy). For the two spin states, spin-unrestricted calculations were performed constraining M_S , the projection of the total electronic spin, to $M_S = +1/2$ and $M_S = +3/2$, for the complex in the LS and HS states, respectively. For the geometry optimization calculations, except for those carried out for the study of the JT instability in the LS state, the symmetry of the complex was constrained to D_3 . For the study of the JT effect in the LS state, the symmetry was lowered to C_2 .

Single crystals of $[\text{Co}(\text{bpy})_3][\text{NaRh}(\text{ox})_3]$ and $[\text{Co}(\text{bpy})_3][\text{LiRh}(\text{ox})_3]$ were grown as described in ref 5 and prepared for the optical measurements as explained in ref 4. The absorption spectra were recorded on a Fourier transform spectrometer equipped with the appropriate light sources, beam splitters, and detectors (Bruker IFS66). Temperatures between 11 and 300 K were achieved with a closed-cycle cryosystem with the sample sitting in He exchange gas (Oxford Instruments CCC 1204). The circular dichroism (CD) spectrum of $[\text{Co}(\text{bpy})_3][\text{LiRh}(\text{ox})_3]$ was recorded at 15 K using the apparatus described in ref 57. For analyzing the spectra of the complex in either spin state, the energy E , the oscillator strength f , and the rotatory strength R of its 80 lowest-lying dipole-allowed electronic excitations were calculated within the adiabatic local density approximation of TDDFT as implemented in the Gaussian package.^{49–52} The calculations were performed at the B3LYP/ \mathcal{G} level on optimized HS and LS geometries obtained at the same theoretical level. The individual absorption and CD bands were simulated by convoluting the oscillator and rotatory strengths with Gaussian functions having a full width at half-maximum of 2000 cm^{-1} . For the CD bands, the normalization of the Gaussian functions is such that⁵⁸

$$R = 22.97 \times 10^{-40} \int dE \frac{\Delta\epsilon(E)}{E} \quad (9)$$

where R is in cgs units; the difference $\Delta\epsilon$ in the extinction coefficients for left- and right-hand circular polarized light is given in $\text{M}^{-1} \text{ cm}^{-1}$.

The oscillator strength f_{ij} and the rotatory strength R_{ij} of an $i \rightarrow j$ transition of energy E_{ij} actually read, in atomic units ($m_e = 1$, $e = 1$, $\hbar = 1$, $4\pi\epsilon_0 = 1$, $c \approx 137.036$),

$$f_{ij} = \frac{2}{3} E_{ij} |\mu_{ij}|^2 \quad (10)$$

where $\mu_{ij} = \langle i|\mu|j\rangle$ and $\mathbf{m}_{ij} = \langle i|\mathbf{m}|j\rangle$ are the electric and

$$R_{ij} = \text{Im}(\mu_{ij} \cdot \mathbf{m}_{ji})$$

magnetic transition dipole moment vectors, respectively. The magnetic dipole moment operator is given by $\mathbf{m} = (-i/2c)\mathbf{r} \times \nabla$. The electric dipole moment operator is given in the dipole-length form by $\mu = -\mathbf{r}$, and in the dipole-velocity form, its matrix elements read $\mu_{ij} = -(1/E_{ij})\nabla_{ij}$. The two representations are equivalent in a complete basis set, but

Table 1. Comparison between Experimental and Optimized HS 4A_2 [Co(bpy) $_3$] $^{2+}$ Geometries

		ADF						
	exp. ^a	PBE/ <i>f</i> ^c	OPBE/ <i>f</i> ^c	RPBE/ <i>f</i> ^c	OLYP/ <i>f</i> ^c			
Bond Lengths [Å]								
Co–N	2.123	2.141	2.149	2.180	2.155			
N–C ₂	1.350	1.359	1.350	1.365	1.355			
N–C ₆	1.338	1.347	1.339	1.352	1.343			
C ₂ –C ₃	1.386	1.401	1.397	1.408	1.400			
C ₃ –C ₄	1.381	1.393	1.387	1.398	1.390			
C ₄ –C ₅	1.364	1.395	1.390	1.401	1.393			
C ₅ –C ₆	1.369	1.392	1.387	1.397	1.389			
C ₂ –C ₂ [′]	1.488	1.480	1.475	1.489	1.480			
Angles [deg]								
<i>β</i>	77.4	76.7	76.0	76.6	75.9			
<i>γ</i>	0.5	4.4	4.3	4.5	4.5			
<i>τ</i>	47.7	50.7	50.5	50.8	50.1			
<i>θ</i>	58.6	60.2	60.6	60.3	60.5			
Gaussian								
	PBE/ <i>g</i>	PBE0/ <i>g</i>	B3LYP/ <i>g</i>	B3LYP [*] / <i>g</i>	O3LYP/ <i>g</i>	HCTH/ <i>g</i>	VSXC/ <i>g</i>	TPSS/ <i>g</i>
Bond Lengths [Å]								
Co–N	2.145	2.156	2.182	2.173	2.139	2.187	2.143	2.148
N–C ₂	1.360	1.344	1.350	1.352	1.343	1.351	1.352	1.360
N–C ₆	1.347	1.334	1.339	1.340	1.332	1.338	1.346	1.347
C ₂ –C ₃	1.402	1.391	1.395	1.397	1.389	1.397	1.396	1.400
C ₃ –C ₄	1.393	1.385	1.388	1.389	1.382	1.386	1.395	1.392
C ₄ –C ₅	1.396	1.386	1.389	1.390	1.383	1.388	1.402	1.395
C ₅ –C ₆	1.393	1.384	1.387	1.388	1.381	1.386	1.392	1.391
C ₂ –C ₂ [′]	1.481	1.480	1.485	1.484	1.472	1.479	1.481	1.480
Angles [deg]								
<i>β</i>	76.7	76.1	75.8	76.0	76.4	75.4	78.0	76.5
<i>γ</i>	4.5	5.2	4.8	4.8	5.0	4.2	33.3	4.1
<i>τ</i>	50.9	50.5	49.9	50.1	50.8	50.1	58.6	51.1
<i>θ</i>	60.3	60.5	60.5	60.452	60.4	60.8	63.0	60.5

^a Experimental values from ref 4.

there are issues tied to their use in finite basis sets.^{52,59–61} Indeed, the dipole-length representation gives origin-dependent rotatory strengths, which is not the case for the dipole-velocity form. This latter form, however, gives rotatory strengths which are sensitive to the quality of the wave functions. In the present case, the two representations have been employed. We only present the results obtained with the dipole-length representation, which generally gives more reliable results.⁶¹

3. Geometry and Energetics of [Co(bpy) $_3$] $^{2+}$

3.1. [Co(bpy) $_3$] $^{2+}$ in the HS State. The calculations carried out for the study of the D_3 complex in the HS state led to its characterization in the 4A_2 and 4E states, which result from the trigonal splitting of the octahedral HS $^4T_{1g}$ state. The 4A_2 state proves to be the lower-lying trigonal component of the HS state. This was also evidenced experimentally.³ Because of the difference in the way they handle orbitally degenerate states, ADF actually allowed the characterization of the complex in both states whereas Gaussian was restricted to the 4A_2 state.

3.1.1. Optimized HS Geometries. 3.1.1.1. The 4A_2 State. Table 1 gives selected bond lengths and the values for the

angles β , γ , τ , and θ (see Figure 2) for the optimized 4A_2 geometries. The experimental values included in Table 1 are taken from the X-ray crystal structure reported for [Co(bpy) $_3$]-[NaCr(ox) $_3$].⁴ In this oxalate network, [Co(bpy) $_3$] $^{2+}$ has a C_3 site symmetry. The experimental values are averaged such that they can be compared to those calculated in D_3 symmetry.

Table 1 shows that, with the exception of the VSXC/ \mathcal{G} results, the optimized parameter values are consistent with one another and compare well with the experimental values. This is, in particular, the case for the Co–N bond length. As experimentally observed, the N–C₂ bond remains longer than the N–C₆ bond. Similarly, the optimized values of the angular parameters are close to the experimental values. This indicates that the arrangement of the ligands around the metal is well-described in the optimized geometries. It is noteworthy that the geometries obtained with the PBE GGA and the \mathcal{J} and \mathcal{G} basis sets are very close to each other, emphasizing the previously reported⁴² equivalence of the STO and GTO basis sets. Generally, the optimized HS geometries are slightly more expanded than experimentally observed. The minor differences can be ascribed to the absence of counterion and packing effects in gas-phase calculations.

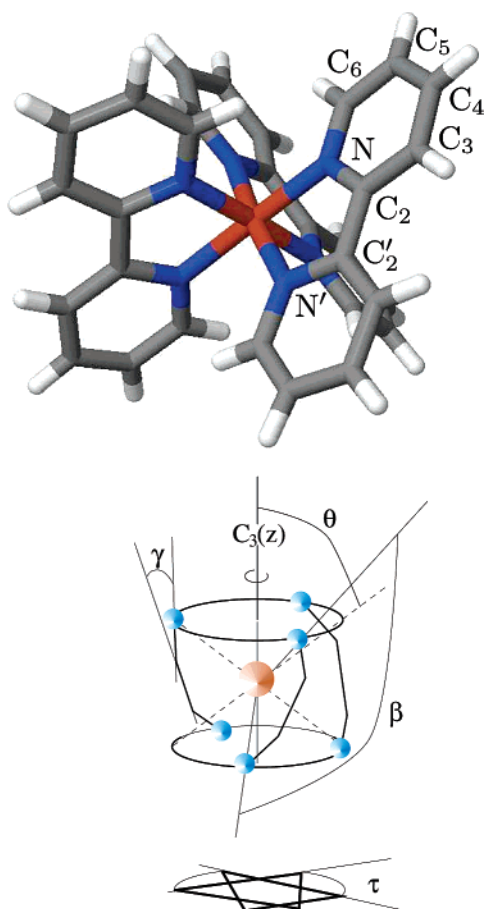


Figure 2. Atom labeling used for the D_3 $[\text{Co}(\text{bpy})_3]^{2+}$ complex (top) and angles characterizing the arrangement of the ligands around the cobalt center (bottom): β is the bite angle, γ the dihedral angle between the ligand moieties, τ the twist angle, and θ the angle between the z axis and the generator of the cone on which the nitrogen atoms are located.

Frequency calculations performed with the Gaussian package show that the geometries obtained with this package are true minima because no imaginary frequency was found. Hence, because of the consistency between the geometries obtained with both Gaussian and ADF, it can be concluded that the above results indeed describe the most stable geometry of $[\text{Co}(\text{bpy})_3]^{2+}$ in the $^4\text{A}_2$ state. The VSXC geometry markedly differs from the experimental and other calculated HS geometries by its angular parameter values (see Table 1 and Figure 3). The ligands are very much twisted and this in a way that favors π stacking of the neighboring pyridinyl rings. This is a direct consequence of the known tendency of the VSXC functional to overestimate long-range interactions such as π - π interactions.^{43,62,63} Therefore, the VSXC functional is not adequate for the description of the geometric structure for the type of transition-metal complex considered here.

3.1.1.2. The ^4E State. Table 2 gives the geometrical parameters of the ^4E HS state calculated using ADF. The comparison of these data with those obtained at the same theoretical levels for the $^4\text{A}_2$ state (see Table 1) shows that the geometries of the complex in the two components of the HS are very similar.

The lack of significant geometrical change in passing from

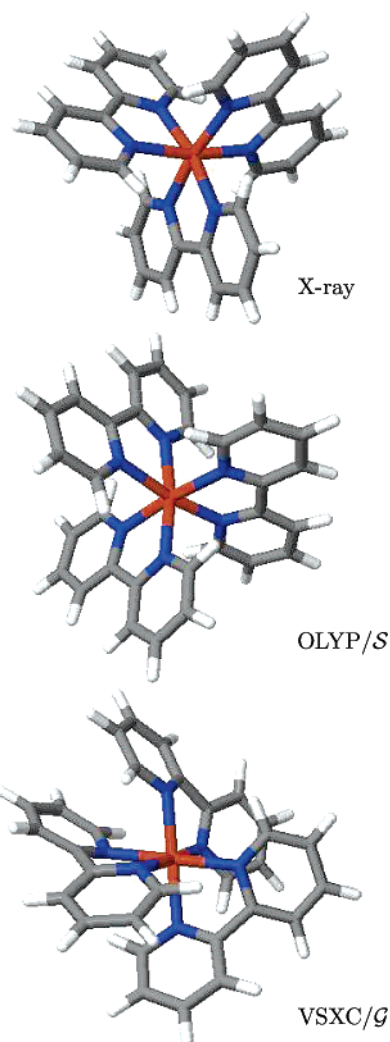


Figure 3. X-ray crystal structure⁴ and optimized OLYP/ \mathcal{S} and VSXC/ \mathcal{G} geometries of the HS $[\text{Co}(\text{bpy})_3]^{2+}$ complex.

Table 2. Optimized HS ^4E $[\text{Co}(\text{bpy})_3]^{2+}$ Geometries (ADF Results)

	PBE/ \mathcal{S}	OPBE/ \mathcal{S}	RPBE/ \mathcal{S}	OLYP/ \mathcal{S}
Bond Lengths [Å]				
Co-N	2.141	2.149	2.180	2.159
N-C ₂	1.359	1.352	1.365	1.356
N-C ₆	1.347	1.340	1.353	1.344
C ₂ -C ₃	1.401	1.398	1.407	1.401
C ₃ -C ₄	1.393	1.388	1.399	1.391
C ₄ -C ₅	1.395	1.390	1.400	1.393
C ₅ -C ₆	1.392	1.388	1.397	1.390
C ₂ -C _{2'}	1.479	1.476	1.490	1.482
Angles [deg]				
β	76.7	75.9	75.8	76.0
γ	4.9	4.7	5.0	4.8
τ	50.3	50.1	49.7	50.1
θ	60.0	60.5	60.4	60.5

one quartet component to the other stems from the fact that, upon inspection of the KS orbital levels, passing from the $^4\text{A}_2$ state to the ^4E state involves the transfer of an of electron from the metallic e_t spin-down orbital level of $\text{Co}(t_{2g})$ parentage to the metallic a_{1t} spin-down orbital level of the

Table 3. Calculated $E(^4E) - E(^4A_2)$ Energy Differences (cm^{-1}) Obtained with ADF

	$E(^4E) - E(^4A_2)$
PBE/ <i>f</i>	1968
OPBE/ <i>f</i>	2000
RPBE/ <i>f</i>	2194
OLYP/ <i>f</i>	1848

same $\text{Co}(t_{2g})$ parentage. Indeed, upon the $O_h \rightarrow D_3$ symmetry lowering, the octahedral metallic t_{2g} level splits into a_1 and e levels, and the occupation of the spin-down orbital levels for the 4A_2 state is $(e_1)^2(a_{11})^0$, and that for the 4E state is $(e_1)^1(a_{11})^1$. These levels are nonbonding, which explains why no significant variation in the geometry of the complex is expected.

3.1.2. The Trigonal Splitting in the HS State. Table 3 gives the values found for the electronic energy difference between the 4E and 4A_2 HS components at the respective optimized geometries. All four functionals predict that the 4A_2 component is lower in energy than the 4E component. The calculated energy differences range from 1848 to 2194 cm^{-1} . However, this spread is comparatively small, all of the functionals predicting a trigonal splitting of about 2000 cm^{-1} . This value is in reasonable agreement with the experimental estimate of 1000 cm^{-1} obtained from the fitting of the magnetization data of the HS $[\text{Co}(\text{bpy})_3](\text{ClO}_4)_2$ compound.³

The 4E state is JT unstable.⁶⁴ However, given that this instability is due to the partial occupation of the degenerate metallic nonbonding e orbital level of $\text{Co}(t_{2g})$ parentage, this is not expected to have a significant influence on the results obtained for the energetics of the HS state. As will be discussed below, this is not the case for the LS 2E state, for which the JT instability results from the single occupation of the doubly degenerate metallic antibonding orbital level of octahedral $\text{Co}(e_g)$ parentage.

3.2. $[\text{Co}(\text{bpy})_3]^{2+}$ in the LS State. This section first presents the results obtained for the characterization of the LS 2E state of $[\text{Co}(\text{bpy})_3]^{2+}$ in the high-symmetry D_3 point group. This is followed by a discussion of the JT instability in this state.

3.2.1. LS 2E Geometries in D_3 . Table 4 shows selected bond lengths and the values of the angles β , γ , τ , and θ found for the optimized LS 2E geometries. The experimental data are taken from the X-ray crystal structure⁴ of the spin-crossover compound $[\text{Co}(\text{bpy})_3][\text{LiCr}(\text{ox})_3]$ at 10 K, where $[\text{Co}(\text{bpy})_3]^{2+}$ is effectively in the LS state. This compound is isostructural with $[\text{Co}(\text{bpy})_3][\text{NaCr}(\text{ox})_3]$, with a C_3 site symmetry for $[\text{Co}(\text{bpy})_3]^{2+}$. The optimized values are again very consistent among the functionals used, and they are in good agreement with the experimental values. We may conclude that the LS structure is described well enough by the different functionals and may thus be used to discuss the structural changes upon spin-state transition. The most important feature to be noticed is that the LS \rightarrow HS transition is characterized by a lengthening of the Co–N bonds by ~ 0.10 Å, which is due to the promotion of an electron from the nonbonding metallic levels of t_{2g} parentage to the antibonding metallic level of e_g parentage. Concomitantly,

Table 4. Comparison between Experimental and Optimized LS 2E Geometries (ADF Results)

	exp. ^a	PBE/ <i>f</i>	OPBE/ <i>f</i>	RPBE/ <i>f</i>	OLYP/ <i>f</i>
Bond Lengths [Å]					
Co–N	2.024	2.039	2.031	2.079	2.063
N–C ₂	1.343	1.362	1.355	1.368	1.359
N'–C ₆	1.338	1.346	1.342	1.354	1.346
C ₂ –C ₃	1.399	1.400	1.397	1.407	1.400
C ₃ –C ₄	1.388	1.393	1.387	1.398	1.391
C ₄ –C ₅	1.373	1.396	1.391	1.401	1.393
C ₅ –C ₆	1.389	1.392	1.388	1.398	1.390
C ₂ –C _{2'}	1.481	1.480	1.466	1.480	1.474
Angles [deg]					
β	80.1	79.9	79.6	78.9	79.0
γ	0.1	6.0	6.1	5.6	6.4
τ	51.2	52.4	52.7	51.9	53.2
θ	58.1	58.7	59.0	59.2	59.2

^a Experimental results taken from ref 4.

there is a marked rearrangement of the ligands around the metal ion, manifesting itself by quite large changes in the angular parameters (see Tables 1 and 4).

3.2.2. The Jahn–Teller Instability in the LS State. A complete study of $[\text{Co}(\text{bpy})_3]^{2+}$ in the LS state requires that one also takes into account the JT instability⁶⁴ due to the orbital degeneracy of the LS 2E state. Even though the X-ray structure shows no evidence for a symmetry lowering for the LS state, electron paramagnetic resonance (EPR) spectra indicate that a dynamic or statically disordered JT effect must be operative.⁶⁵

For such a large molecular system as $[\text{Co}(\text{bpy})_3]^{2+}$ with numerous (177) vibrational degrees of freedom, the JT effect⁶⁴ in the LS 2E state is probably a multimode one. That is, it may involve the coupling of the 2-fold degenerate electronic state to several vibrational modes of a_1 , a_2 , or e symmetries, according to the decomposition $E \otimes E = A_1 + A_2 + E$, which gives the symmetries of the vibrational modes that could couple linearly to the 2E state. For displacements along an a_1 vibrational mode, the full D_3 symmetry of the complex is preserved, and for displacements along an a_2 mode, the C_3 symmetry is maintained. Thus, only the e modes can be JT-active and lift the orbital degeneracy. For a full discussion of the JT effect and the many aspects of vibronic interactions, see refs 66–70. In the following, we restrict ourselves to the characterization of the extrema of low symmetry on the LS adiabatic potential energy surface (APES). Therefore, the geometry of the complex was optimized while constraining the symmetry of the molecular framework to C_2 . This led to the identification of two extrema, which correspond to electronic states of 2A and 2B symmetry. The vibrational analysis performed for the 2A and 2B geometries revealed zero and one imaginary frequency, respectively. The vibrational mode of imaginary frequency found for the 2B geometry is of b symmetry and transforms the 2B geometry into the 2A geometry. Consequently, the 2A geometry corresponds to a minimum and the 2B geometry to a saddle point between two such minima. The trigonal symmetry of the JT problem implies that there actually exist three equivalent minima and three associated equivalent saddle points. Additionally, the presence of the saddle points

Table 5. Selected Distances (Å) and Angles (deg) Characterizing the JT-Distorted Geometry of $[\text{Co}(\text{bpy})_3]^{2+}$ at the Minima (A) and Saddle Points (B) of the LS APES

Part A									
	L1				L2				
	Co–N = Co–N'	C ₂ –C ₂ '	β	γ	Co–N	Co–N'	C ₂ –C ₂ '	β	γ
ADF Results									
PBE/ <i>f</i>	1.956	1.464	82.2	0.5	1.982	2.191	1.475	78.7	11.5
OPBE/ <i>f</i>	1.950	1.457	81.8	3.4	1.972	2.209	1.472	78.0	5.3
RPBE/ <i>f</i>	1.990	1.471	81.5	3.6	2.015	2.252	1.486	77.5	4.3
OLYP/ <i>f</i>	1.980	1.464	81.4	3.5	2.005	2.243	1.479	77.4	5.3
Gaussian Results									
PBE/ <i>g</i>	1.959	1.464	82.1	0.4	1.985	2.190	1.476	78.7	11.9
PBE0/ <i>g</i>	1.982	1.468	81.6	0.0	2.000	2.218	1.477	77.9	10.1
B3LYP/ <i>g</i>	2.004	1.472	81.2	0.0	2.027	2.256	1.483	77.3	10.1
B3LYP*/ <i>g</i>	1.993	1.470	81.5	0.1	2.016	2.244	1.482	77.7	10.1
O3LYP/ <i>g</i>	1.953	1.457	82.1	0.0	1.974	2.199	1.469	78.4	10.8
HCTH/ <i>g</i>	1.974	1.460	81.6	0.1	2.011	2.261	1.475	77.3	12.4
TPSS/ <i>g</i>	1.961	1.464	82.1	0.4	1.987	2.193	1.476	78.6	11.5
Part B									
	L1				L2				
	Co–N = Co–N'	C ₂ –C ₂ '	β	γ	Co–N	Co–N'	C ₂ –C ₂ '	β	γ
ADF Results									
PBE/ <i>f</i>	2.129	1.477	77.3	13.9	1.935	2.057	1.467	81.2	3.7
OPBE/ <i>f</i>	2.172	1.473	75.6	17.3	1.925	2.063	1.463	80.6	0.1
RPBE/ <i>f</i>	2.202	1.486	75.8	18.5	1.959	2.094	1.476	80.5	1.8
OLYP/ <i>f</i>	2.188	1.480	75.7	17.7	1.947	2.083	1.469	80.4	0.2
Gaussian Results									
PBE/ <i>g</i>	2.131	1.478	77.3	14.3	1.938	2.059	1.468	81.2	3.9
PBE0/ <i>g</i>	2.142	1.479	76.7	11.2	1.956	2.091	1.472	80.4	3.0
B3LYP/ <i>g</i>	2.178	1.484	76.0	11.1	1.988	2.122	1.477	79.8	3.1
B3LYP*/ <i>g</i>	2.167	1.483	76.3	11.4	1.969	2.105	1.475	80.3	3.0
O3LYP/ <i>g</i>	2.123	1.471	77.1	12.1	1.929	2.062	1.461	80.9	3.5
HCTH/ <i>g</i>	2.193	1.478	75.5	14.8	1.952	2.091	1.465	80.4	3.9
TPSS/ <i>g</i>	2.128	1.478	77.2	13.8	1.941	2.061	1.468	81.0	4.1

indicates that quadratic vibronic coupling is effective. Thus, assuming that the JT instability is well-described by an ideal single-mode $E \otimes e$ problem, the section of the LS APES along the effective e mode resembles the warped Mexican hat potential.⁷¹

3.2.2.1. JT-Distorted Geometries of $[\text{Co}(\text{bpy})_3]^{2+}$ at the Minima and the Saddle Points. In these geometries, one ligand (L1) lies on the C_2 axis and is left unchanged by the C_2 rotation, contrarily to the other two ligands (L2), which are interchanged by this operation. In the L1 ligand moiety, the two Co–N bond lengths are the same, while for L2, they differ. Parts A and B of Table 5 give the Co–N and C₂–C₂' bond lengths and the values of the angles β and γ calculated with all of the previously used functionals (with the exception of the VSXC functional) for the ²A and ²B geometries, respectively. All functionals predict very similar geometries for the complex at the minima and at the saddle points. There is also a nice match between the values obtained at the PBE/*f* and PBE/*g* levels for the structural parameters, which illustrates the equivalence of these GTO and STO basis sets.

From the comparison of the structural data given in Tables 4 and 5, the JT distortion to which the geometry of the

complex is subjected in going from the D_3 apex to one of the minima can be depicted as follows. Starting from the D_3 geometry, one ligand moves closer to the cobalt atom. Its displacement takes place along the C_2 axis in such a way that its local C_2 symmetry is preserved. For this ligand, which will be designated L1, the shortening of the Co–N bonds amounts to ~ 0.08 Å. The other two ligands undergo rearrangements while remaining equivalent to the C_2 rotation that leaves L1 unchanged. For each of these two ligands, designated L2, one Co–N bond shortens by ~ 0.07 Å while the other lengthens by ~ 0.17 Å. Compared to L1, the Co–N bonds in L2 are longer by ~ 0.02 – 0.03 Å for one of the pyridinyl moieties and by ~ 0.24 – 0.27 Å for the other. The larger distance of the L2 ligands to the cobalt is accompanied by a lengthening of the C₂–C₂' bonds by ~ 0.01 Å, a decrease of the bite angle β by about 4° , and a generalized increase of the dihedral angle γ , which helps maintain optimal metal–ligand orbital interactions.

The distortion that brings $[\text{Co}(\text{bpy})_3]^{2+}$ from its high-symmetry configuration to its geometry at one of the saddle points can be described in the same manner. In this case, however, the L1 ligand moves away from the metal atom,

Table 6. Low-Spin [Co(bpy)₃]²⁺ Complex: Values of the Co–N Bond Length in *D*₃ Symmetry and Averaged Values of the Co–N Bond Lengths in *C*₂ Symmetry (ADF Results)

	PBE/ <i>f</i>	OPBE/ <i>f</i>	RPBE/ <i>f</i>	OLYP/ <i>f</i>
<i>D</i> ₃	2.039	2.031	2.079	2.063
<i>C</i> ₂ (av.)	2.042	2.049	2.085	2.074

Table 7. Calculated Values of the JT Stabilization Energy *E*_{JT} and Barrier Height Δ^a

	<i>E</i> _{JT} [cm ⁻¹]	Δ [cm ⁻¹]
ADF Results		
PBE/ <i>f</i>	1542	308
OPBE/ <i>f</i>	1443	391
RPBE/ <i>f</i>	1466	419
OLYP/ <i>f</i>	1483	334
Gaussian Results		
PBE/ <i>G</i>		304
PBE0/ <i>G</i>		342
B3LYP/ <i>G</i>		282
B3LYP*/ <i>G</i>		320
O3LYP/ <i>G</i>		383
HCTH/ <i>G</i>		354
TPSS/ <i>G</i>		-45 (311)

^a The value given in parentheses for the TPSS functional was obtained using the “ultrafine” integration grid (see text).

which leads to a ~0.10 Å increase of its Co–N bond lengths. As for the L2 ligands, their rearrangement translates into the shortening of one Co–N bond by about 0.11 Å and into a lengthening of the other by ~0.02 Å. The Co–N bond length in L1 is about 2.13–2.20 Å; it is larger than the two different Co–N bond lengths of L2 by ~0.07 Å and ~0.20 Å. L1 being the most distant ligand to the cobalt, it exhibits a smaller bite angle, a slightly larger C₂–C₂' distance, and a larger dihedral angle γ than those of L2.

In the solid state, the JT distortion can be less than predicted because of the steric constraints imposed by the environment of the complex. If the JT effect is static, then there is a disorder of the JT distortion over the three *C*₂ axes, which explains the high symmetry of the X-ray structure of LS [Co(bpy)₃]²⁺. If the JT effect is dynamic, then, on the time scale of the X-ray measurements, the quantum-mechanical zero-point delocalization of the complex around the moat of the LS APES averages out the instantaneous JT distortions. From the discussion above, the average value of the Co–N bond lengths in *C*₂ symmetry is expected to be quite close to the value of the single Co–N bond length in *D*₃ symmetry. That this is indeed the case is confirmed in Table 6.

3.2.2.2. The Energetics of the JT Effect. The energetic terms in the JT effect are the JT stabilization energy *E*_{JT}, which is the energy difference between the *D*₃ apex and the global minimum of the LS APES, and the height Δ of the energy barrier between the minima, which is the energy difference between the minima and the saddle points. The values found for these two energetic parameters are summarized in Table 7. All functionals give for either parameter very consistent values, with deviations that fall within the chemical accuracy of 350 cm⁻¹ (~1 kcal/mol).

The negative Δ value obtained with the TPSS meta-GGA corresponds to an unphysical description of the LS APES wherein the global minima are higher in energy than the saddle points. It is, however, well-known that the meta-GGAs are sensitive to the integration grid.⁶² For the TPSS functional, the results obtained for the JT energetics can be significantly improved by using the “ultrafine” integration grid in Gaussian in place of the smaller default grid. This leaves the optimized geometries unchanged, but the calculated energy barrier now amounts to Δ = 311 cm⁻¹, in very good agreement with the values obtained with the other functionals. In summary:

$$E_{\text{JT}} \approx 1500 \text{ cm}^{-1}; \Delta \approx 340 \text{ cm}^{-1} \quad (12)$$

Further insight into the JT effect requires the determination of the JT-active modes and the characterization of the LS APES along each of the JT modes in order to determine their respective contributions to *E*_{JT} and Δ. This is a work in progress.

3.2.2.3. The Nature of the JT Effect. A static JT effect requires high barriers along each of the JT modes; that is, one must verify^{69,71} $\delta_i \gg \hbar\omega_i$ (*i* = 1, ..., *p*), where ω_i is the angular frequency and δ_i the contribution to Δ of the *i*th JT-active mode. Given that the JT distortions in the LS state mainly involve drastic changes in the Co–N bond lengths, the JT-active modes have to be among the vibrational modes which involve the Co–N bonds. For the complex in the HS state, the results of our vibrational analysis show that the frequencies of such modes are in the 110–270 cm⁻¹ range, in agreement with the proposed identification of Co–N stretching modes in the far-infrared region.⁷² The vibrational analysis similarly performed for the geometries found for the *C*₂ minima of the LS APES gives the frequencies of such modes in the 110–360 cm⁻¹ range (for calculated vibrational frequencies for [Co(bpy)₃]²⁺, see the Supporting Information). It is therefore reasonable to assume that the frequencies $\hbar\omega_i$ (*i* = 1, ..., *p*) of the JT-active modes are in the same 110–360 cm⁻¹ interval. Because the value found for Δ provides an upper bound for the δ_i 's, it turns out that, for any JT-active mode “*i*”, δ_i is on the same order of magnitude as the vibrational quantum $\hbar\omega_i$: $\delta_i \lesssim \hbar\omega_i$, (*i* = 1, ..., *p*). The condition for a static JT effect clearly is not obeyed.

3.3. The High-Spin/Low-Spin Energy Difference. Because the isolated [Co(bpy)₃]²⁺ complex has a HS ground state, the zero-point energy difference between the HS and the LS state is negative:

$$\Delta E_{\text{HL}}^{\circ} = E_{\text{HS}}^{\circ} - E_{\text{LS}}^{\circ} < 0. \quad (13)$$

This inequality can therefore be used as a criterion to assess the functionals with regard to their ability to correctly predict the ground state. The zero-point energies *E*[°] are calculated as the sum of the electronic and vibrational contributions, *E*^{el} and *E*^{vib}, respectively. *E*^{el} is obtained from the geometry optimization, while *E*^{vib} can be accessed from the vibrational analysis performed on the optimized geometries within the harmonic approximation.

Given that the HS state is split by the trigonal field, the relevant zero-point energy in this spin state must equal that

Table 8. Calculated HS–LS Electronic Energy Differences^a

	$\Delta E_{\text{HL}}^{\text{el}}$ [cm ⁻¹]
ADF Results	
PBE/ <i>f</i>	3919
OPBE/ <i>f</i>	893
RPBE/ <i>f</i>	1526
OLYP/ <i>f</i>	334
Gaussian Results	
PBE/ <i>f</i>	3836
PBE0/ <i>f</i>	-3212
B3LYP/ <i>f</i>	-2076
B3LYP*/ <i>f</i>	-543
O3LYP/ <i>f</i>	168
HCTH/ <i>f</i>	-596
TPSS/ <i>f</i>	2781(2847)

^a The value given in parentheses was obtained by using the "ultrafine" integration grid.

of the lowest-lying trigonal component 4A_2 : $E_{\text{HS}}^{\circ} = E^{\circ}(^4A_2)$. As for the JT-unstable LS state, the zero-point energy is the one evaluated at the JT distorted minima of C_2 symmetry: $E_{\text{LS}}^{\circ} = E^{\circ}(^2A)$. An additional correction to the calculated LS zero-point energy must be considered when one is to treat the dynamic nature of the JT instability.⁷¹ However, this can be expected to be a minor correction to the ground vibronic level of the LS state as given by $E^{\circ}(^2A)$. Hence, this correction can be neglected. The HS–LS zero-point energy difference can, in turn, be separated into its electronic $\Delta E_{\text{HL}}^{\text{el}}$ and vibrational $\Delta E_{\text{HL}}^{\text{vib}}$ contributions according to $\Delta E_{\text{HL}}^{\circ} = \Delta E_{\text{HL}}^{\text{el}} + \Delta E_{\text{HL}}^{\text{vib}}$. The vibrational analyses performed using the Gaussian package give a $\Delta E_{\text{HL}}^{\text{vib}}$ value of between -330 and -110 cm⁻¹ depending on the functional used. Its minus sign reflects the weakening of the cobalt–ligand bond upon the LS \rightarrow HS change of spin states. Using for $\Delta E_{\text{HL}}^{\text{vib}}$ the average value of -200 cm⁻¹, the criterion given by eq 13 now reads

$$\Delta E_{\text{HL}}^{\text{el}} < -\Delta E_{\text{HL}}^{\text{vib}} \approx 200 \text{ cm}^{-1} \quad (14)$$

The calculated values of $\Delta E_{\text{HL}}^{\text{el}}$ given in Table 8 show that most functionals do not fulfill this condition. Indeed, the different functionals give very different values for $\Delta E_{\text{HL}}^{\text{el}}$, ranging from -3212 cm⁻¹ (PBE0) to 3919 cm⁻¹ (PBE). This large spread contrasts with the consistency observed when comparing the results obtained for the HS and LS geometries of the complex (with the exception of the discarded VSXC functional) and for the energetics of the JT effect in the LS state as well as for the trigonal splitting in the HS state. Thus, consistency among the functionals is achieved for the description of the geometry of the complex in either spin state. However, when it comes to energetics, consistency is retained only when comparing results for a given spin multiplicity, and large deviations are observed when dealing with different spin states. The values obtained with the PBE functional show a remarkable consistency between the results obtained with the GTO *f*-basis set in Gaussian and the STO *f*-basis set in ADF. The equivalence of these two basis sets was already established when treating geometrical parameters. The consistency observed for the spin-state energetics

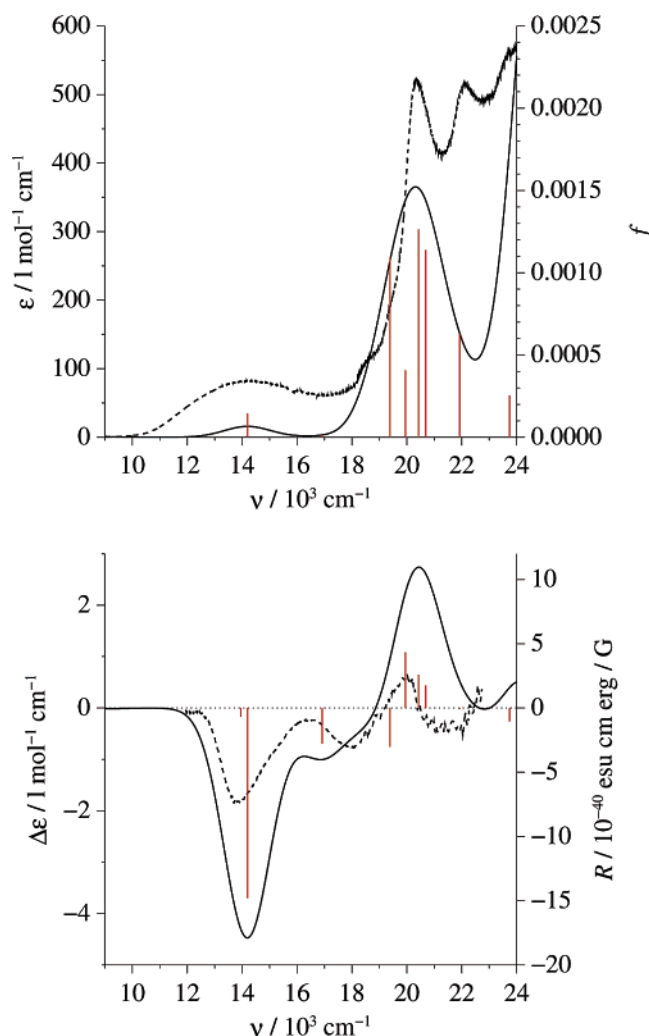


Figure 4. Calculated absorption (top) and CD (bottom) spectra of LS Λ -[Co(bpy)₃]²⁺. The experimental single-crystal absorption and CD spectra of [Co(bpy)₃][LiRh(ox)₃], recorded at 11 and 15 K, respectively, are shown (dashed lines) for comparison.

fully validates the comparison of results from these two basis sets notably when using the Gaussian and ADF packages.

In line with previous observations,^{40–42} the spin-state energetics provide a very stringent criterion for assessing the performance of the approximate functionals. The PBE, RPBE, and OPBE GGAs and the TPSS meta-GGA functionals fail to correctly predict the HS state as the ground state of the isolated [Co(bpy)₃]²⁺ complex. With $\Delta E_{\text{HL}}^{\text{el}}$ values of between 893 and 3919 cm⁻¹, these semilocal functionals overestimate the stability of the LS state with regard to the HS state. The OLYP and HCTH GGAs whose $\Delta E_{\text{HL}}^{\text{el}}$ values are 334 and -596 cm⁻¹, respectively, correctly predict the HS state to be the ground state or at least to be almost equienergetic with the LS state. Compared to the other semilocal functionals, their built-in nonlocality overcomes the tendency of their LDA component to destabilize states of higher multiplicities and thus to overestimate the HS–LS energy difference. As for the hybrids, they all predict the correct ground state. The PBE0, B3LYP, B3LYP*, and O3LYP functionals give $\Delta E_{\text{HL}}^{\text{el}}$ values of -3212, -2076, -543, and 168 cm⁻¹, respectively. Their exact

Table 9. Excitation Energies, Oscillator Strengths, Rotational Strengths for the Λ -Enantiomer, and Assignments Calculated for $[\text{Co}(\text{bpy})_3]^{2+}$ in the LS ^2A State

excited state	E [cm^{-1}]	f [$\times 10^{-5}$]	R [10^{-40} cgs]	major MO \rightarrow MO transitions	main character
^2B	3790	0.18	-0.076	$69a_1 \rightarrow 69b_1$ (33%) $69a_1 \rightarrow 71b_1$ (29%) $69a_1 \rightarrow 72b_1$ (18%)	d-d ^a
^2A	5203	0.09	-0.052	$65b_1 \rightarrow 69b_1$ (40%) $66b_1 \rightarrow 71b_1$ (29%) $66b_1 \rightarrow 72b_1$ (18%)	d-d ($^2\text{T}_1$, $^2\text{T}_2$)
^2B	6823	20.90	1.139	$70a_1 \rightarrow 69b_1$ (89%)	d-d ($^2\text{T}_1$, $^2\text{T}_2$)
^2B	8738	0.18	-0.095	$66a_1 \rightarrow 69b_1$ (38%) $67a_1 \rightarrow 71b_1$ (11%) $68a_1 \rightarrow 71b_1$ (20%) $68a_1 \rightarrow 72b_1$ (12%)	d-d ($^2\text{T}_1$, $^2\text{T}_2$)
^2A	13951	0.01	-0.680	$65b_1 \rightarrow 69b_1$ (11%) $69a_1 \rightarrow 74a_1$ (70%)	d-d ($^2\text{T}_1$, $^2\text{T}_2$)
^2B	14196	14.51	-14.795	$69a_1 \rightarrow 69b_1$ (11%) $66b_1 \rightarrow 74a_1$ (64%) $69a_1 \rightarrow 71b_1$ (10%)	d-d ($^2\text{T}_1$, $^2\text{T}_2$)
^2B	16917	1.25	-2.789	$66a_1 \rightarrow 69b_1$ (42%) $67a_1 \rightarrow 71b_1$ (11%) $68a_1 \rightarrow 71b_1$ (19%) $68a_1 \rightarrow 72b_1$ (12%)	d-d + MLCT
^2B	19383	108.96	-2.973	$70a_1 \rightarrow 67b_1$ (61%) $66b_1 \rightarrow 74a_1$ (16%) $69a_1 \rightarrow 71b_1$ (9%)	MLCT
^2A	19953	40.75	4.333	$65b_1 \rightarrow 69b_1$ (17%) $66b_1 \rightarrow 71b_1$ (25%) $66b_1 \rightarrow 72b_1$ (15%) $69a_1 \rightarrow 74a_1$ (31%)	d-d + MLCT
^2B	20426	126.37	2.586	$70a_1 \rightarrow 67b_1$ (51%) $66b_1 \rightarrow 74a_1$ (27%) $69a_1 \rightarrow 71b_1$ (10%)	MLCT
^2A	20690	113.86	1.762	$70a_1 \rightarrow 71a_1$ (97%)	MLCT
^2B	21924	62.59	-0.080	$70a_1 \rightarrow 68b_1$ (94%)	MLCT
^2B	23746	25.36	-1.059	$67a_1 \rightarrow 67b_1$ (9%) $69a_1 \rightarrow 67b_1$ (10%) $66a_1 \rightarrow 67b_1$ (16%) $69a_1 \rightarrow 67b_1$ (51%)	MLCT + intraligand
^2A	24541	464.05	3.846	$67a_1 \rightarrow 74a_1$ (18%) $68a_1 \rightarrow 74a_1$ (33%) $66b_1 \rightarrow 67b_1$ (40%)	MLCT

^a Transition toward the highest sheet of the LS adiabatic potential energy surface (see JT effect).

exchange contributions amount to 25, 20, 15, and 11.61%, respectively. That is, the HS-LS energy difference calculated within the hybrid formalism decreases with an increasing amount of exact exchange. However, hybrids with large exact-exchange contributions such as the B3LYP and PBE0 clearly overestimate the stability of the HS state with regard to the LS state in transition-metal complexes, and this can be remedied by reducing this contribution to $\sim 10\%$.^{37,38,42} In conclusion, the B3LYP* and O3LYP hybrids as well as the OLYP and HCTH GGAs give the best results regarding the calculation of the HS-LS energy difference in the isolated $[\text{Co}(\text{bpy})_3]^{2+}$ complex.

4. Photophysical Properties

In the characterization of $[\text{Co}(\text{bpy})_3]^{2+}$, the absorption and circular dichroism spectra are significant signatures for the

population of the different states of the complex. In the following, they are analyzed on the basis of TDDFT calculations carried out at the B3LYP/ \mathcal{G} level.

4.1 $[\text{Co}(\text{bpy})_3]^{2+}$ in the LS State. Figure 4 shows the single-crystal absorption spectrum of the spin-crossover compound $[\text{Co}(\text{bpy})_3][\text{LiRh}(\text{ox})_3]$, which has been recorded at 10 K where $[\text{Co}(\text{bpy})_3]^{2+}$ is in the LS state. The slightly asymmetric band centered at $14\,000\text{ cm}^{-1}$ was previously attributed to the spin-allowed and overlapping d-d transitions of the low-spin species, namely, the $^2\text{E}(\text{t}_{2g}^6\text{e}_g^1) \rightarrow ^2\text{T}_1(\text{t}_{2g}^5\text{e}_g^2)$, $^2\text{T}_2(\text{t}_{2g}^5\text{e}_g^2)$ transitions according to the Tanabe-Sugano diagram for octahedral d^7 complexes. The higher-energy bands were likewise attributed to d-d transitions,³ but this assignment was later questioned.⁴ The electronic excitation calculations were performed using the JT-distorted C_2 geometry of the complex in the ^2A state. Figure 4 shows

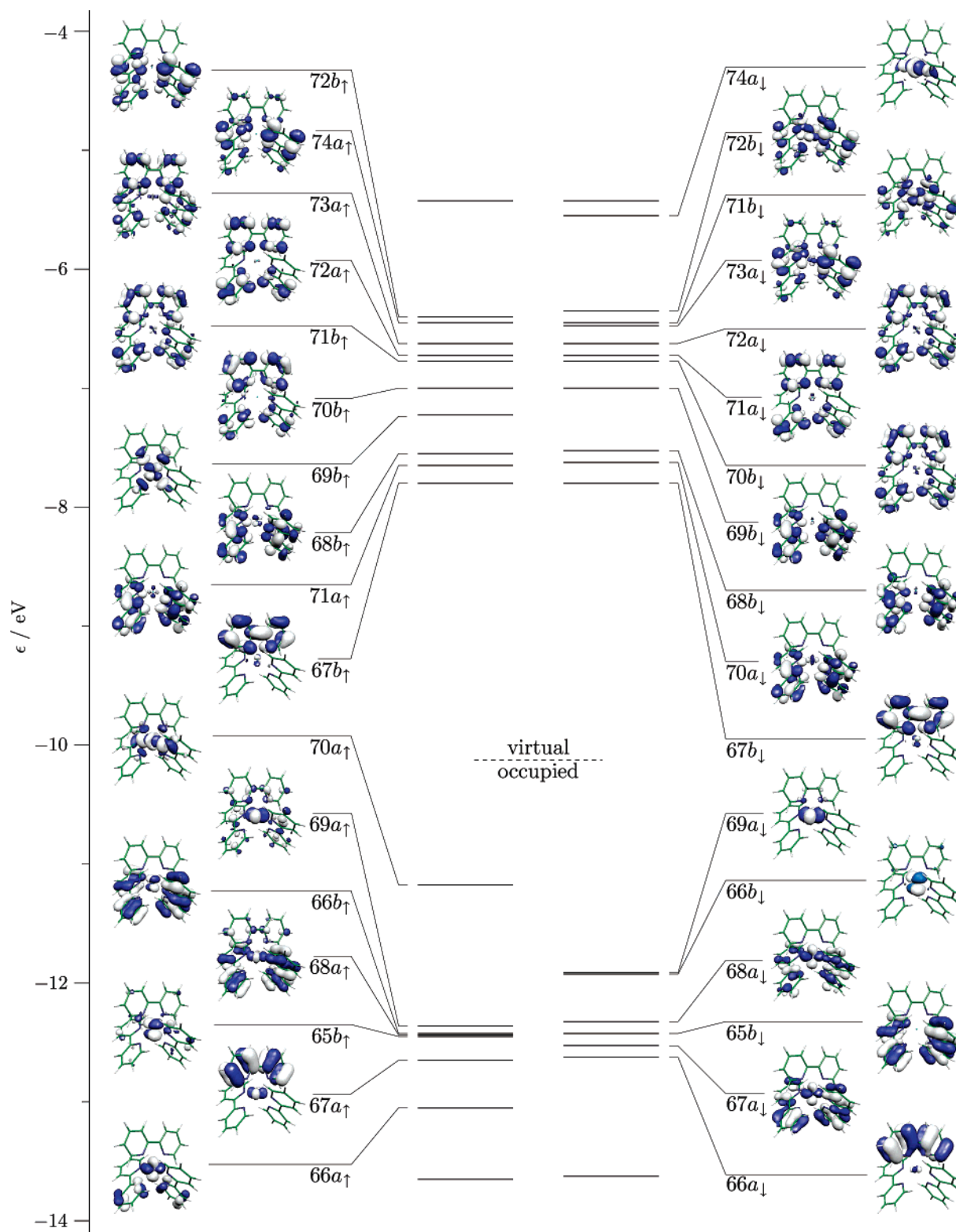


Figure 5. Frontier KS MOs of the C_2 complex $[\text{Co}(\text{bpy})_3]^{2+}$ in the LS 2A state (B3LYP/ \mathcal{S} results).

the stick plot of the calculated oscillator strengths along with the plot of the simulated absorption spectrum. Although there are some differences in the intensities, the relative intensities of the experimental absorption bands are well-reproduced and the maxima of the measured and calculated absorption bands coincide to within $\sim 1000 \text{ cm}^{-1}$, which leads to a very good overall agreement between the experimental and the predicted spectra.

In going from the O_h to the C_2 symmetry, the d-d transitions predicted for $[\text{Co}(\text{bpy})_3]^{2+}$ on the basis of LFT considerations split as follows. The $^2E \rightarrow ^2T_1$ transition decomposes into a $^2A \rightarrow ^2A$ and two $^2A \rightarrow ^2B$ transitions, and the $^2E \rightarrow ^2T_2$ transition decomposes into two $^2A \rightarrow ^2A$ and a $^2A \rightarrow ^2B$ transition. We thus expect to identify six corresponding d-d transitions in the calculated spectra. Additionally, with the LS 2E state being split into the 2A

and 2B states due to the Jahn–Teller effect, we also expect a lower-energy intraconfigurational transition corresponding to the $^2A \rightarrow ^2B$ excitation. The characteristics of all the calculated spin-allowed transitions of interest are given in Table 9. This includes the excitation energies, the oscillator strengths, and the rotational strengths for the Λ -enantiomer as well as the assignments of these transitions. The assignments were made on the basis of the diagram of the frontier KS molecular orbitals (MOs) in Figure 5 in order to identify the major mono-electronic MO \rightarrow MO excitations contributing to a given transition.

In Table 9, the lowest-lying transition at 3790 cm^{-1} corresponds to the intraconfigurational $^2A \rightarrow ^2B$ transition. However, it has comparatively low oscillator strength and has not been identified experimentally so far. It is likewise difficult to identify all six of the transitions of $^2E \rightarrow ^2T_1$, 2T_2 parentage. Three of them are expected in the range between 5000 and 9000 cm^{-1} , but only one of them carries significant oscillator strength. It has not yet been observed experimentally either. Two such transitions are predicted at about $14\,000\text{ cm}^{-1}$, one of them carrying significant oscillator strength. Thus, we may indeed attribute the experimental absorption band at this energy to a d–d transition. At higher energy, the transitions are strongly mixed, carrying both d–d and metal-to-ligand charge-transfer (MLCT) characters, but the most intense transitions in the region around $20\,000\text{ cm}^{-1}$ are predominantly MLCT transitions.

CD spectroscopy constitutes a versatile tool to elucidate the nature of electronic transitions in chiral complexes. $[\text{Co}(\text{bpy})_3][\text{LiRh}(\text{ox})_3]$ crystallizes in the chiral and cubic space group $P2_13$ with spontaneous resolution of the racemate.⁴ Figure 4 shows the single-crystal CD spectrum of this compound at 15 K . It also includes the results of the TDDFT calculations performed for the Λ -enantiomer, namely, the stick plot of the rotatory strengths and the plot of the simulated CD spectrum. The calculated and experimental CD spectra present a very good agreement from which one can infer the configuration of the complex in the crystal; that is, in the crystal under investigation, the complexes are present as the Λ - $[\text{Co}(\text{bpy})_3]^{2+}$ enantiomer. d–d transitions have usually comparatively large CD intensities, whereas MLCT transitions have smaller intensities with respect to their molar extinction coefficients. The fact that above $18\,000\text{ cm}^{-1}$ the values of the relative CD signals expressed as $\Delta\epsilon/\epsilon_{\text{max}}$ are lower than 0.002 as compared to the value of 0.02 for the signals at $14\,000\text{ cm}^{-1}$ corroborates the assignments of the high-energy bands to MLCT transitions. It is noteworthy that the electronic transition predicted at $16\,917\text{ cm}^{-1}$ has a very weak oscillator strength but carries a relatively large CD intensity. Although the analysis based on the MOs led to the conclusion that it exhibits both an MLCT character and a d–d character, the last observations suggest that this transition may predominantly be viewed as a higher-lying d–d transition.

4.2. $[\text{Co}(\text{bpy})_3]^{2+}$ in the HS State. Figure 6 shows the single-crystal absorption spectrum of the HS compound $[\text{Co}(\text{bpy})_3][\text{LiRh}(\text{ox})_3]$ measured at 12 K . The experimental absorption band at $11\,500\text{ cm}^{-1}$ was assigned to the spin-allowed d–d transition $^4T_1(t_{2g}^5e_g^2) \rightarrow ^4T_2(t_{2g}^4e_g^3)$.⁴

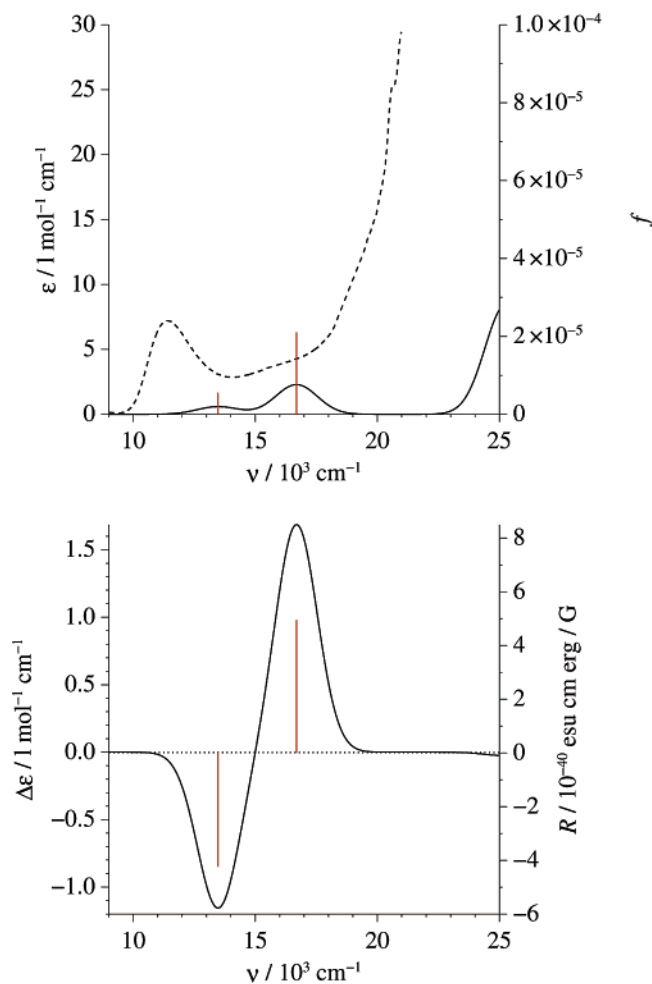


Figure 6. Calculated absorption (top) and CD (bottom) spectra of HS Λ - $[\text{Co}(\text{bpy})_3]^{2+}$. The 12 K single-crystal absorption spectrum of $[\text{Co}(\text{bpy})_3][\text{NaRh}(\text{ox})_3]$ is shown (dashed line) for comparison purposes (see text).

The TDDFT calculations were carried out using the D_3 geometry of $[\text{Co}(\text{bpy})_3]^{2+}$ in the HS 4A_2 state. In the effective D_3 symmetry of the complex, because of the trigonal splitting of the HS 4T_1 and 4T_2 states, one expects to identify a $^4A_2 \rightarrow ^4A_1$ and a $^4A_2 \rightarrow ^4E$ transition in addition to a $^4A_2 \rightarrow ^4E$ intraconfigurational transition at lower energy. Table 10 gives for the spin-allowed transitions of interest the excitation energies, the oscillator strengths, and the rotational strengths for the Λ -enantiomer. It also gives their assignments, which are based on the MO diagram of Figure 7. The intraconfigurational transition is calculated at 3203 cm^{-1} and has not been observed so far. The two components $^4A_2 \rightarrow ^4A_1$, 4E of the d–d $^4T_1 \rightarrow ^4T_2$ transition are predicted at $13\,473$ and $16\,687\text{ cm}^{-1}$, respectively. The dipole-forbidden d–d transition at $20\,403\text{ cm}^{-1}$ corresponds to an excitation toward the 4A_2 trigonal component of the LFT $^4T_1(t_{2g}^5e_g^2)$ state.

The absorption and CD spectra simulated using these results are plotted in Figure 6. The calculated absorption spectrum does not agree with the experimental spectrum on an absolute energy scale. However, it very nicely predicts the region with no absorption band before the rise of a relatively intense band corresponding to an intraligand π – π^* transition (Table 10). The shift in energy of $\sim 4000\text{ cm}^{-1}$ between the experimental and calculated spectra indicates

Table 10. Excitation Energies, Oscillator Strengths, Rotational Strengths for the Λ -Enantiomer, and Assignments Calculated for $[\text{Co}(\text{bpy})_3]^{2+}$ in the HS $^4\text{A}_2$ State

state	$E [\text{cm}^{-1}]$	$f [\times 10^{-5}]$	$R [10^{-40} \text{ cgs}]$	major MO \rightarrow MO transitions	main character
^4E	3203	0.40	4.900	$43e_i \rightarrow 25a_{1i} (15\%)$ $44e_i \rightarrow 25a_{1i} (66\%)$	d-d (HS $^4\text{T}_1$ state) ^a
$^4\text{A}_1$	13473	0.51	-4.215	$43e_i \rightarrow 48e_i (18\%)$ $44e_i \rightarrow 48e_i (74\%)$	d-d ($^4\text{T}_2$)
^4E	16687	1.05	2.476	$43e_i \rightarrow 48e_i (16\%)$ $44e_i \rightarrow 48e_i (74\%)$	d-d ($^4\text{T}_2$)
$^4\text{A}_2$	20403	0.00	0.000	$43e_i \rightarrow 48e_i (16\%)$ $44e_i \rightarrow 48e_i (74\%)$	d-d ($^4\text{T}_1$)
^4E	25255	3.16	0.047	$25a_{1i} \rightarrow 46e_i (15\%)$ $44e_i \rightarrow 46e_i (15\%)$ $44e_i \rightarrow 23a_{2i} (15\%)$ $24a_{1i} \rightarrow 45e_i (14\%)$ $43e_i \rightarrow 45e_i (10\%)$ $43e_i \rightarrow 23a_{2i} (11\%)$	intraligand ($\pi-\pi^*$)

^a Trigonal component of the HS state.

an overestimation of the excitation energies of the allowed and forbidden transitions in the near-IR/visible domain. This also implies for the two transitions $^4\text{A}_2 \rightarrow ^4\text{A}_1$, ^4E that only the latter has been observed experimentally.

The discrepancy between the calculated and experimental excitation energies could be due to the fact that, in carrying out the calculations in D_3 , we do not consider the possibility of a pseudo-JT effect between the close-lying $^4\text{A}_2$ and JT-unstable ^4E components of the HS state. This is being investigated.

5. Concluding Remarks

Density-functional theory has been applied to the study of the structural, energetic, and photophysical properties of $[\text{Co}(\text{bpy})_3]^{2+}$ in the HS and LS states. The structural and energetic features of the complex in each spin state were thus determined by carrying out geometry optimizations using several GGA (PBE, OPBE, RPBE, OLYP, and HCTH), meta-GGA (VSXC and TPSS), and hybrid (B3LYP, B3LYP*, O3LYP, and PBE0) functionals in combination with the STO- \mathcal{J} and GTO- \mathcal{G} basis sets. Its electronic absorption and CD spectra were likewise analyzed on the basis of the results of TDDFT calculations performed at the B3LYP/ \mathcal{G} level. The main results and conclusions obtained can be summarized as follows.

Calculations performed with the PBE functional and the two basis sets gave almost identical results, thus validating the direct comparison of results from both basis sets.⁴² With the exception of the VSXC functional, all of the functionals perform equally well with regard to the description of the geometry of the complex and with regard to its energetics in a given spin multiplicity. The VSXC functional gives unphysical geometries because of its well-known tendency toward the overestimation of long-range bonding interactions,^{43,62,63} and it therefore cannot be expected to give reliable results for the energetics of the complex even within the same spin multiplicity. The TPSS meta-GGA does give correct geometries, but an integration grid higher than usual must be used for it to give reliable results for the energetics.

Density-functional calculations carried out in D_3 symmetry allowed the characterization of the complex in the LS ^2E

state of the octahedral $^2\text{E}(t_{2g}^6 e_g^1)$ parentage and in the HS $^4\text{A}_2$ and ^4E states of the octahedral $^4\text{T}_1(t_{2g}^5 e_g^2)$ parentage. The $^4\text{A}_2$ state is found to be the lower-lying trigonal component of the HS state, as observed experimentally, and the trigonal splitting is estimated to be $\sim 2000 \text{ cm}^{-1}$, in reasonable agreement with the experimental value of 1000 cm^{-1} .³ There is no significant structural change in passing from one quartet component to the other because this principally involves an electronic rearrangement within nonbonding metallic levels of octahedral $\text{Co}(t_{2g})$ parentage. The calculated ^2E and $^4\text{A}_2$ geometries agree well with the X-ray crystal structures⁴ of the complex in either spin state. The lengthening of the Co-N bonds by $\sim 0.10 \text{ \AA}$ observed upon the LS \rightarrow HS transition can be ascribed to the fact that the change of spin states involves the promotion of an electron from a nonbonding metallic level of octahedral $\text{Co}(t_{2g})$ parentage into an antibonding metallic level of octahedral $\text{Co}(e_g)$ parentage.

The JT instability of the LS ^2E state was investigated by determining the extrema of low symmetry (C_2) of the LS APES. Two extrema could be identified, which correspond to the ^2A and ^2B states and which are a true minimum and a saddle point, respectively. Because of the trigonal symmetry of the JT problem, there are three such minima and three such saddle points. In addition, the presence of the saddle points shows that the JT effect involves quadratic vibronic coupling. The geometries of $[\text{Co}(\text{bpy})_3]^{2+}$ in the ^2A and ^2B states are different, each being characterized by distinct variations in the Co-N bond lengths and ligand arrangement with respect to the high-symmetry configuration. The JT stabilization energy and the height of the barrier to pseudorotation amount to $E_{\text{JT}} \approx 1500 \text{ cm}^{-1}$ and $\Delta \approx 340 \text{ cm}^{-1}$, respectively. The theoretical results support the idea of a dynamic JT instability in the LS state, which can be inferred from the high symmetry of the X-ray crystal structure of LS $[\text{Co}(\text{bpy})_3]^{2+}$ ⁴ and its EPR spectra.⁶⁵

The spin-state energetics prove to be the most stringent criterion for assessing the performance of the functionals. To correctly give the HS state as the ground state of the isolated $[\text{Co}(\text{bpy})_3]^{2+}$ complex, the calculated values of the HS-LS energy difference $\Delta E_{\text{HL}}^{\text{el}}$ must verify $\Delta E_{\text{HL}}^{\text{el}} \lesssim$

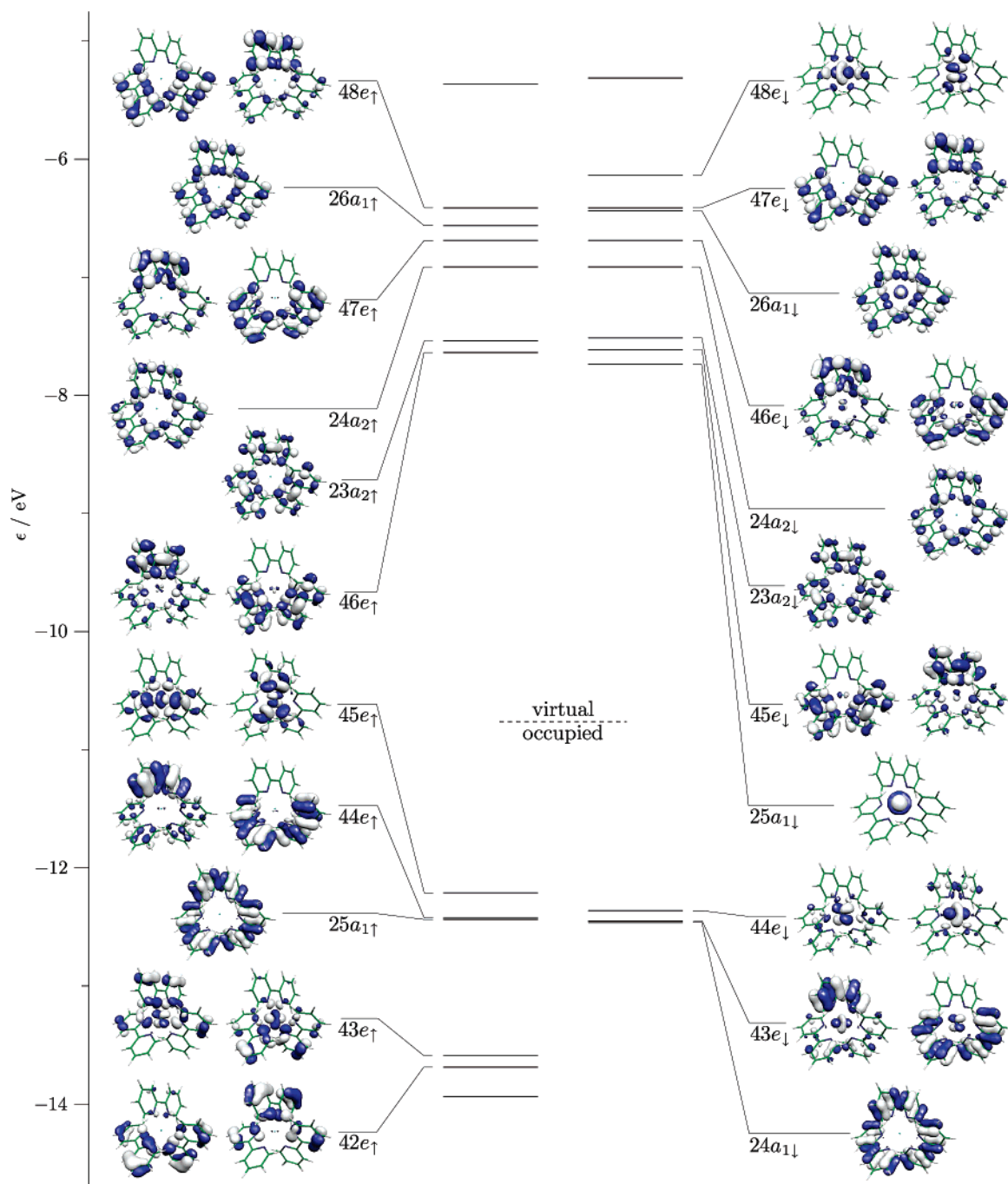


Figure 7. Frontier KS MOs of the D_3 complex $[\text{Co}(\text{bpy})_3]^{2+}$ in the HS 4A_2 state (B3LYP/ \mathcal{G} results).

$-\Delta E_{\text{HL}}^{\text{vib}} \approx 200 \text{ cm}^{-1}$. However, this criterion is not met by all of the functionals despite the fact that they all perform equally well for the geometry of the complex and for its energetics within a given spin multiplicity. Of all the functionals tested, the OLYP and HCTH GGAs and the B3LYP* and O3LYP hybrids give the best performance with $\Delta E_{\text{HL}}^{\text{el}}$ values of 334, -596 , -543 , and 168 cm^{-1} , respectively, that is, around zero as expected for a complex close to the spin-crossover point.

The absorption and CD spectra deduced from the calculated oscillator and rotatory strengths based on TDDFT are in very good agreement with the experimental spectra. This allows a clear-cut assignment of the observed electronic transitions and of the chirality of the complex in the sample studied by CD spectroscopy. For the study of the photo-

physical properties of the complex in the HS state, the TDDFT calculations were performed using the geometry of D_3 symmetry found for $[\text{Co}(\text{bpy})_3]^{2+}$ in the 4A_2 state. Although the calculated absorption spectrum for the near-IR/visible region proves to be very similar in shape to the experimental one, it presents a shift toward higher energies by some $\sim 4000 \text{ cm}^{-1}$. This discrepancy is tentatively ascribed to the neglect of the pseudo-JT effect between the two trigonal components of the HS state.

In summary, the present theoretical study has allowed us to gain new insight into the structural, energetic, and photophysical properties of the $[\text{Co}(\text{bpy})_3]^{2+}$ complex in the LS and HS states. Among the 11 state-of-the-art functionals that have been used, only four prove to perform well for the HS–LS energy difference in the isolated complex. These

functionals, namely, the OLYP, HCTH, B3LYP*, and O3LYP functionals, are therefore good candidates for the study of the guest–host interactions that are responsible for turning the HS complex into a spin-crossover system.

Acknowledgment. This work has benefitted from the financial support of the Swiss National Science Foundation and the MAGMANet NoE of the European Union (contract NMP3-CT-2005-515767-2). We acknowledge supercomputer time at the Centro Svizzero di Calcolo Scientifico (CSCS) in the framework of the CSCS project entitled “Photophysics and Photochemistry of Transition Metal Compounds: Theoretical Approaches”. We thank Claudio Redaelli, Angelo Mangili, Claudio Bareato, and Djordje Maric of the CSCS for valuable technical support. We also thank Pierre-Yves Morgantini and Mihail Atanasov for helpful discussions.

Supporting Information Available: Tables S1 and S2 list calculated vibrational frequencies for $[\text{Co}(\text{bpy})_3]^{2+}$ in the HS $^4\text{A}_2$ state and in the LS ^2A state, respectively (PBE/6-311G and B3LYP*/6-311G results). For comparison purposes, Table S1 also gives the IR frequencies experimentally determined for the HS species by Saito et al.⁷² The calculated IR spectra of the complex in the two spin states are shown in Figure S1. This material is available free of charge via the Internet at <http://pubs.acs.org>.

References

- (1) Mizuno, K.; Lunsford, J. H. Electron Paramagnetic Resonance Study of Tris(2,2'-bipyridine)cobalt(II) Complexes in Zeolite Y: Evidence for Spin Equilibrium. *Inorg. Chem.* **1983**, *22*, 3484–3486.
- (2) Tiwary, S. K.; Vasudevan, S. Spin Crossover in the Ship-in-a-Bottle Compound: Cobalt(II)tris(bipyridyl) Encapsulated in Zeolite-Y. *Chem. Phys. Lett.* **1997**, *277*, 84–88.
- (3) Tiwary, S. K.; Vasudevan, S. Void Geometry Driven Spin Crossover in Zeolite-Encapsulated Cobalt Tris(bipyridyl) Complex Ion. *Inorg. Chem.* **1998**, *37*, 5239–5246.
- (4) Sieber, R.; Decurtins, S.; Stoeckli-Evans, H.; Wilson, C.; Yufit, D.; Howard, J. A. K.; Capelli, S. C.; Hauser, A. A Thermal Spin Transition in $[\text{Co}(\text{bpy})_3][\text{LiCr}(\text{ox})_3]$ (ox = $\text{C}_2\text{O}_4^{2-}$; bpy = 2, 2'-bipyridine. *Chem.-Eur. J.* **2000**, *361*–368.
- (5) Zerara, M.; Hauser, A. Cobalt(II)-tris-2,2'-bipyridine as a Spin-Crossover Complex: Evidence for Cooperative Effects in Three-Dimensional Oxalate Networks. *ChemPhysChem* **2004**, *5*, 395–399.
- (6) Hauser, A.; Amstutz, N.; Delahaye, S.; Sadki, A.; Schenker, S.; Sieber, R.; Zerara, M. Fine Tuning the Electronic Properties of $[\text{M}(\text{bpy})_3]^{2+}$ Complexes by Chemical Pressure (M = Fe^{2+} , Ru^{2+} , Co^{2+} ; bpy = 2,2'-Bypyridine). *Struct. Bonding* **2004**, *106*, 81–96.
- (7) Hohenberg, P.; Kohn, W. Inhomogeneous Electron Gas. *Phys. Rev.* **1964**, *136*, B864–B871.
- (8) Kohn, W.; Sham, L. J. Self-Consistent Equations Including Exchange and Correlation Effects. *Phys. Rev.* **1965**, *140*, A1133–A1138.
- (9) Gunnarsson, O.; Lundqvist, B. I. Exchange and Correlation in Atoms, Molecules, and Solids by the Spin-Density-Functional Formalism. *Phys. Rev. B: Solid State* **1976**, *13*, 4274–4298.
- (10) Parr, R. G.; Yang, W. *Density-Functional Theory of Atoms and Molecules*; Oxford University Press: New York, 1989.
- (11) Dreizler, R. M.; Gross, E. K. U. *Density Functional Theory, An Approach to the Quantum Many-Body Problem*; Springer-Verlag: New York, 1990.
- (12) Koch, W.; Holthausen, M. C. *A Chemist's Guide to Density Functional Theory*; Wiley-VCH: New York, 2000.
- (13) Ceperley, D. M.; Adler, B. J. Ground State of the Electron Gas by a Stochastic Method. *Phys. Rev. Lett.* **1980**, *45*, 566–569.
- (14) Vosko, S. H.; Wilk, L.; Nusair, M. Accurate Spin-Dependent Electron Liquid Correlation Energies for Local Spin Density Calculations: A Critical Analysis. *Can. J. Phys.* **1980**, *58*, 1200–1211.
- (15) Wang, Y.; Perdew, J. P. Correlation Hole of the Spin-Polarized Gas, with Exact Small-Wave-Vector and High-Density Scaling. *Phys. Rev. B: Condens. Matter Mater. Phys.* **1991**, *44*, 13298–13307.
- (16) Perdew, J. P.; Wang, Y. Accurate and Simple Analytic Representation of the Electron-Gas Correlation. *Phys. Rev. B: Condens. Matter Mater. Phys.* **1992**, *45*, 13244–13249.
- (17) Ma, S.-K.; Brueckner, K. E. Correlation Energy of an Electron Gas with a Slowly Varying High Density. *Phys. Rev.* **1968**, *165*, 18–31.
- (18) Langreth, D. C.; Mehl, M. J. Beyond the Local-Density Approximation in Calculations of Ground-State Electronic Properties. *Phys. Rev. B: Condens. Matter Mater. Phys.* **1983**, *28*, 1809–1834.
- (19) Perdew, J. P. Density-Functional Approximation for the Correlation Energy of the Inhomogeneous Gas. *Phys. Rev. B: Condens. Matter Mater. Phys.* **1986**, *33*, 8822–8824.
- (20) Becke, A. D. Density-Functional Exchange Energy Approximation with Correct Asymptotic Behavior. *Phys. Rev. A: At., Mol., Opt. Phys.* **1988**, *38*, 3098–3100.
- (21) Becke, A. D. Simulation of Delocalized Exchange by Local Density Functionals. *J. Chem. Phys.* **2000**, *112*, 4020–4026.
- (22) Nekovee, M.; Foulkes, W. M. C.; Needs, R. J. Quantum Monte Carlo Analysis of Exchange and Correlation in the Strongly Inhomogeneous Electron Gas. *Phys. Rev. Lett.* **2001**, *87*, 036401.
- (23) Tao, J.; Perdew, J. P.; Staroverov, V. N.; Scuseria, G. E. Climbing the Density Functional Ladder: Nonempirical Meta-Generalized Gradient Approximation Designed for Molecules and Solids. *Phys. Rev. Lett.* **2003**, *91*, 146401.
- (24) Cancio, A. C.; Chou, M. Y. Beyond the Local Approximation to Exchange and Correlation: The Role of the Laplacian of the Density in the Energy Density of Si. <http://xxx.lanl.gov/pdf/cond-mat/0506462> (accessed Dec 2005).
- (25) Becke, A. D. A New Mixing of Hartree–Fock and Local Density-Functional Theories. *J. Chem. Phys.* **1993**, *98*, 1372–1377.
- (26) Becke, A. D. Density-Functional Thermochemistry. III. The Role of Exact Exchange. *J. Chem. Phys.* **1993**, *98*, 5648–5652.
- (27) Perdew, J. P.; Ernzerhof, M.; Burke, K. Rationale for Mixing Exact Exchange with Density Functional Approximations. *J. Chem. Phys.* **1996**, *105*, 9982–9985.
- (28) Ernzerhof, M. Construction of the Adiabatic Connection. *Chem. Phys. Lett.* **1996**, *263*, 499–506.

- (29) Burke, K.; Ernzerhof, M.; Perdew, J. P. The Adiabatic Connection Method: A Non-empirical Hybrid. *Chem. Phys. Lett.* **1997**, *265*, 115–120.
- (30) Becke3LYP Method References and General Citation Guidelines. *Gaussian NEWS*; Gaussian, Inc.: Wallingford, CT; Vol 5, no. 2, summer 1994, p 2.
- (31) Adamo, C.; Barone, V. Toward Reliable Density Functional Methods without Adjustable Parameters: The PBE0 Model. *J. Chem. Phys.* **1999**, *110*, 6158–6170.
- (32) Ernzerhof, M.; Scuseria, G. E. Assessment of the Perdew–Burke–Ernzerhof Exchange–Correlation Functional. *J. Chem. Phys.* **1999**, *110*, 5029–5036.
- (33) Lee, C.; Yang, W.; Parr, R. G. Development of the Colle–Salvetti Correlation–Energy Formula into a Functional of the Electron Density. *Phys. Rev. B: Condens. Matter Mater. Phys.* **1988**, *37*, 785–789.
- (34) Perdew, J. P.; Burke, K.; Ernzerhof, M. Generalized Gradient Approximation Made Simple. *Phys. Rev. Lett.* **1996**, *77*, 3865–3868.
- (35) Perdew, J. P.; Burke, K.; Ernzerhof, M. Erratum: Generalized Gradient Approximation Made Simple. *Phys. Rev. Lett.* **1996**, *77*, 3865; *Phys. Rev. Lett.* **1997**, *78*, 1396 Errata.
- (36) Paulsen, H.; Duelund, L.; Winkler, H.; Toftlund, H.; Trautwein, A. X. Free Energy of Spin-Crossover Complexes Calculated with Density Functional Methods. *Inorg. Chem.* **2001**, *40*, 2201–2204.
- (37) Reiher, M.; Salomon, O.; Hess, B. A. Reparameterization of Hybrid Functionals Based on Energy Differences of State of Different Multiplicity. *Theor. Chem. Acc.* **2001**, *107*, 48–55.
- (38) Salomon, O.; Reiher, M.; Hess, B. A. Assertion and Validation of the Performance of the B3LYP^{*} Functional for the First Transition Metal Row and the G2 Test Set. *J. Chem. Phys.* **2002**, *117*, 4729–4737.
- (39) Reiher, M. Theoretical Study of the Fe(phen)₂(NCS)₂ Spin-Crossover Complex with Reparametrized Density Functionals. *Inorg. Chem.* **2002**, *41*, 6928–6935.
- (40) Fouqueau, A.; Mer, S.; Casida, M. E.; Lawson Daku, L. M.; Hauser, A.; Mineva, T. Comparison of Density Functionals for Energy and Structural Differences between the High- $[^5T_{2g}: (t_{2g})^4(e_g)^2]$ and Low- $[^1T_1: (t_{2g})^6(e_g)^0]$ Spin States of the Hexaquoferrous Cation $[\text{Fe}(\text{H}_2\text{O})_6]^{2+}$. *J. Chem. Phys.* **2004**, *120*, 9473–9486.
- (41) Fouqueau, A.; Casida, M. E.; Lawson Daku, L. M.; Hauser, A.; Neese, F. Comparison of Density Functionals for Energy and Structural Differences between the High- $[^5T_{2g}: (t_{2g})^4(e_g)^2]$ and Low- $[^1T_1: (t_{2g})^6(e_g)^0]$ Spin States of Iron(II) Coordination Compounds: II. Comparison of Results for More than Ten Modern Functionals with Ligand Field Theory and ab Initio Results for the Hexaquoferrous Cation $[\text{Fe}(\text{H}_2\text{O})_6]^{2+}$, and the Hexaminoferrous Cation $[\text{Fe}(\text{NH}_3)_6]^{2+}$. *J. Chem. Phys.* **2005**, *122*, 044110.
- (42) Lawson Daku, L. M.; Vargas, A.; Hauser, A.; Fouqueau, A.; Casida, M. E. Assessment of Density Functionals for the High-Spin/Low-Spin Energy Difference in the Low-Spin Iron(II)tris(2,2'-bipyridine) Complex. *ChemPhysChem* **2005**, *6*, 1393–1410.
- (43) Ganzenmüller, G.; Berkaine, N.; Fouqueau, A.; Casida, M. E.; Reiher, M. Comparison of Density Functionals for Differences between the High- $(^5T_{2g})$ and Low- $(^1A_{1g})$ Spin States of Iron(II) Compounds. IV. Results for the Ferrous Complexes $[\text{Fe}(\text{L})(\text{'NHS}_4\text{'})]$. *J. Chem. Phys.* **2005**, *122*, 234321.
- (44) Hammer, B.; Hansen, L. B.; Nørskov, J. K. Improved Adsorption Energetics within Density-Functional Theory Using Revised Perdew–Burke–Ernzerhof Functionals. *Phys. Rev. B: Condens. Matter Mater. Phys.* **1999**, *59*, 7413–7421.
- (45) Handy, N. C.; Cohen, A. J. Left–Right Correlation Energy. *Mol. Phys.* **2001**, *99*, 403–412.
- (46) Boese, A. D.; Handy, N. C. A New Parametrization of Exchange–Correlation Generalized Gradient Approximation Functionals. *J. Chem. Phys.* **2001**, *114*, 5497–5503.
- (47) Cohen, A. J.; Handy, N. C. Dynamic Correlation. *Mol. Phys.* **2001**, *99*, 607–615.
- (48) Van Voorhis, T.; Scuseria, G. E. A Novel Form for the Exchange–Correlation Energy Functional. *J. Chem. Phys.* **1998**, *109*, 400–410.
- (49) Casida, M. E. Time-Dependent Density Functional Response Theory for Molecules. In *Recent Advances in Density Functional Methods*; Chong, D. P., Ed.; World Scientific: Singapore, 1995; Vol. 1.
- (50) Stratmann, R. E.; Scuseria, G. E.; Frisch, M. J. An Efficient Implementation of Time-Dependent Density Functional Theory for the Calculation of Excitation Energies of Large Molecules. *J. Chem. Phys.* **1998**, *109*, 8218–8224.
- (51) Bauernschmitt, R.; Ahlrichs, R. Treatment of Electronic Excitations within the Adiabatic Approximation of Time Dependent Density Functional Theory. *Chem. Phys. Lett.* **1996**, *256*, 454–464.
- (52) Autschbach, J.; Ziegler, T.; van Gisbergen, S. J. A.; Baerends, E. J. Chiroptical Properties from Time-Dependent Density Functional Theory. I. Circular Dichroism Spectra of Organic Molecules. *J. Chem. Phys.* **2002**, *116*, 6930–6940.
- (53) te Velde, G.; Bickelhaupt, F. M.; Baerends, E. J.; Fonseca Guerra, C.; van Gisbergen, S. J. A.; Snijders, J. G.; Ziegler, T. Chemistry with ADF. *J. Comput. Chem.* **2001**, *22*, 931–967.
- (54) *Amsterdam Density Functional Program*, Release ADF2004.01; Theoretical Chemistry, Vrije Universiteit: Amsterdam, The Netherlands. <http://www.scm.com> (accessed Mar 2006).
- (55) Frisch, M. J.; Trucks, G. W.; Schlegel, H. B.; Scuseria, G. E.; Robb, M. A.; Cheeseman, J. R.; Montgomery, J. A., Jr.; Vreven, T.; Kudin, K. N.; Burant, J. C.; Millam, J. M.; Iyengar, S. S.; Tomasi, J.; Barone, V.; Mennucci, B.; Cossi, M.; Scalmani, G.; Rega, N.; Petersson, G. A.; Nakatsuji, H.; Hada, M.; Ehara, M.; Toyota, K.; Fukuda, R.; Hasegawa, J.; Ishida, M.; Nakajima, T.; Honda, Y.; Kitao, O.; Nakai, H.; Klene, M.; Li, X.; Knox, J. E.; Hratchian, H. P.; Cross, J. B.; Bakken, V.; Adamo, C.; Jaramillo, J.; Gomperts, R.; Stratmann, R. E.; Yazyev, O.; Austin, A. J.; Cammi, R.; Pomelli, C.; Ochterski, J. W.; Ayala, P. Y.; Morokuma, K.; Voth, G. A.; Salvador, P.; Dannenberg, J. J.; Zakrzewski, V. G.; Dapprich, S.; Daniels, A. D.; Strain, M. C.; Farkas, O.; Malick, D. K.; Rabuck, A. D.; Raghavachari, K.; Foresman, J. B.; Ortiz, J. V.; Cui, Q.; Baboul, A. G.; Clifford, S.; Cioslowski, J.; Stefanov, B. B.; Liu, G.; Liashenko, A.; Piskorz, P.; Komaromi, I.; Martin, R. L.; Fox, D. J.; Keith,

- T.; Al-Laham, M. A.; Peng, C. Y.; Nanayakkara, A.; Challacombe, M.; Gill, P. M. W.; Johnson, B.; Chen, W.; Wong, M. W.; Gonzalez, C.; Pople, J. A. *Gaussian 03*, revision B.03/B.04; Gaussian, Inc.: Pittsburgh, PA, 2003.
- (56) Schäfer, A.; Huber, C.; Ahlrichs, R. Fully Optimized Contracted Gaussian Basis Sets of Triple- ζ Valence Quality for Atoms Li to Kr. *J. Chem. Phys.* **1994**, *100*, 5829–5835.
- (57) Årsköld, S. P.; Masters, V. N.; Prince, B. J.; Smith, P. J.; Pace, R. J.; Krausz, E. Optical Spectra of Synechocystis and Spinach Photosystem II Preparations at 1.7 K: Identification of the D1-Pheophytin Energies and Stark Shifts. *J. Am. Chem. Soc.* **2003**, *125*, 13063–13074.
- (58) Schellman, J. A. Circular Dichroism and Optical Rotation. *Chem. Rev.* **1975**, *75*, 323–331.
- (59) Furche, F.; Ahlrichs, R.; Wachsmann, C.; Weber, E.; Sobanski, A.; Vögtle, F.; Grimme, S. Circular Dichroism of Helicenes Investigated by Time-Dependent Density Functional Theory. *J. Am. Chem. Soc.* **2000**, *122*, 1717–1724.
- (60) Liang, W. Z.; Yokojima, S.; Chen, G. H. Localized-Density-Matrix Calculation of Circular Dichroism Spectrum of Optically Active Molecule. *Chem. Phys.* **2003**, *289*, 175–189.
- (61) Diedrich, C.; Grimme, S. Systematic Investigation of Modern Quantum Chemical Methods to Predict Electronic Circular Dichroism Spectra. *J. Phys. Chem. A* **2003**, *107*, 2524–2539.
- (62) Johnson, E. R.; Wolkow, R. A.; DiLabio, G. A. Application of 25 Density Functionals to Dispersion-Bound Homomolecular Dimers. *Chem. Phys. Lett.* **2004**, *394*, 334–338.
- (63) Sancho-García, J. C.; Cornil, J. Assessment of Recently Developed Exchange-Correlation Functionals for the Description of Torsion Potential in π -Conjugated Molecules. *J. Chem. Phys.* **2004**, *121*, 3096–3101.
- (64) Jahn, H. A.; Teller, E. Stability of Polyatomic Molecules in Degenerate Electronic States. *Proc. R. Soc. London, Ser. A* **1937**, *161*, 220–235.
- (65) Zerara, M. Transition de Spin Dans le Complexe Cobalt-(II)tris(2,2'-bipyridine). Ph.D. Thesis, Université de Genève, Genève, Switzerland, 2003; Thesis no. 3445.
- (66) O'Brien, M. C. M.; Chancey, C. C. The Jahn–Teller Effect: An Introduction and Current Review. *Am. J. Phys.* **1993**, *61*, 688–697.
- (67) Ham, F. S. The Jahn–Teller Effect: A Retrospective View. *J. Lumin.* **2000**, *85*, 193–197.
- (68) Bersuker, I. B. Modern Aspects of the Jahn–Teller Effect Theory and Applications To Molecular Problems. *Chem. Rev.* **2001**, *101*, 1067–1114.
- (69) Applegate, B. E.; Barckholtz, T. A.; Miller, T. A. Exploration of Conical Intersections and Their Ramifications for Chemistry through the Jahn–Teller Effect. *Chem. Soc. Rev.* **2003**, *32*, 38–49.
- (70) Sabin, J. R.; Brändas, E.; *Manifestations of Vibronic Coupling in Chemistry and Physics*; Elsevier: Amsterdam, 2003; volume 44 of *Advances in Quantum Chemistry*.
- (71) Bersuker, I. B. *The Jahn–Teller Effect and Vibronic Interactions in Modern Chemistry*; Fackler, J. P., Jr., Ed.; Plenum Press: New York, 1984; Modern Inorganic Chemistry Series.
- (72) Saito, Y.; Takemoto, J.; Hutchinson, B.; Nakamoto, K. Infrared Studies of Coordination Compounds Containing Low-Oxidation-State Metals. I. Tris(2,2'-bipyridine) and Tris-(1,10-phenanthroline) Complexes. *Inorg. Chem.* **1972**, *11*, 2003–2011.

CT6001384